Institute of Geophysics
Polish Academy of Sciences

Limitations of first P-wave onset method of full seismic moment tensor inversion and impact on effective application in anthropogenic seismicity studies

Limity metody inwersji pełnego tensora momentu sejsmicznego z amplitud pierwszych wstąpień fal P oraz ich wpływ na efektywne zastosowanie w badaniach sejsmiczności antropogenicznej.

Anna Tymińska, MSc
PhD dissertation

Supervisor: Grzegorz Lizurek, PhD

Abstract

When an earthquake occurs, we do not know the causes or forces which drive the tremor. To determine earthquake mechanism the seismic moment tensor (MT) is a widely used tool. The non-shearing components of the seismic moment tensor for natural earthquakes could inform about the inaccuracy of the solution. However, for induced events non-double-couple components are an important part of the mechanism. The commonly used method of MT calculations for induced seismic events needs to be examined for sensibility for a wide range of factors. Relevant to correct MT solution are azimuthal coverage and noise, but the distinct influence that factors on MT solution is undetermined. Knowledge about possible errors will allow us to improve MT solutions interpretation.

As the first stage of the research, synthetic tests were carried out, where synthetic amplitudes were generated based on the assumed mechanism, and after adding noise, the mechanism was solved. The tests were carried out for four seismic networks established for anthropogenic seismicity monitoring: Legnica-Głogów Cooper District, Bogdanka mine, Song Tranh 2 reservoir and Lai Chau reservoir. Different mechanisms were analysed, from shear to non-DC under noise levels up to 40% of the initial amplitude. As the first way to improve MT inversion, the possibility of implementing HR-GNSS data to increase the azimuth coverage was checked. The analysed data concerned two shocks with magnitudes M=3.8 and M=4 occurring in the LGCD area. The last stage was to determine the influence of the intermediate field on the amplitudes recorded at stations at different distances from the source based on the networks in LGCD and Song Tranh. The research was based on the assumption of the Haskell model for a shear source and took into account a simplified radiation pattern.

The findings highlight the importance of knowing the velocity model when solving MT and identifying features of the model that can cause errors, like layer boundaries or low-velocity layers. The Lai Chau and Song Tranh networks provide stable and reliable MT solutions, while mine networks Rudna and Bogdanka should not be used for routine MT inversion without extensive tests of variability as shown in this work or *in situ* information. The proposed method of implementing additional data from HR-GNSS demonstrates its usefulness for recording tremors above M=3.5 at close distances, which improves azimuthal coverage. Research on the influence of the intermediate field underscores the significance of this issue and the necessity for further investigation. For seismic stations closer than 10 km to the seismic event, it's worth considering intermediate field term influence. Both methods can improve MT solutions for shallow events observed in short distances, like in mine area monitoring.

Streszczenie

Kiedy następuje trzęsienie ziemi, nie znamy przyczyn ani sił, które je wywołały. Do określenia mechanizmu trzęsienia ziemi szeroko stosowanym narzędziem jest tensor momentu sejsmicznego (MT). Nieścinające składowe tensora momentu sejsmicznego dla naturalnych trzęsień ziemi mogą informować o niedokładności rozwiązania, ale są istotną częścią mechanizmów wstrząsów indukowanych. Powszechnie stosowaną metodę obliczeń MT jaką jest inwersja amplitud pierwszych wstąpień fal P należy zbadać pod kątem wrażliwości na szeroki zakres czynników. Dla prawidłowego rozwiązania MT istotne są pokrycie azymutalne i szum w zapisach sejsmicznych, ale dokładny wpływ tych czynników na rozwiązanie MT jest nieokreślony. Wiedza o błędach pozwoli na zwiększenie dokładności rozwiązań MT.

W pierwszym etapie badań zostały przeprowadzone testy syntetyczne, gdzie na podstawie założonego mechanizmu generowane były syntetyczne amplitudy, których wartość była zaburzana szumem po czym dokonywano inwersji do MT. Testy zostały przeprowadzone dla czterech sieci założonych w celu monitoringu sejsmiczności antropogenicznej: w Legnicko-Głogowskim Okręgu Miedziowym, kopalni Bogdanka, zbiornikach Song Tranh 2 i Lai Chau. Analizowane były różne mechanizmy oraz poziomy szumu. Następnie sprawdzono czy zastosowanie wysokoczęstotliwościowych danych GNSS w celu zwiększenia pokrycia azymutalnego wpływa na jakość inwersji MT. Wykonano to na przykładzie dwóch wstrząsów o magnitudach M=3.8 oraz M=4, które wystąpiły w obszarze LGOM i miały dostępne dane GNSS pozwalające na ich użycie w analizie MT. Ostatnim etapem było określenie poziomu wpływu pola pośredniego na amplitudy rejestrowane na stacjach sieci w LGOM i Song Tranh. Badania oparte były na założeniu modelu Haskell'a dla źródła ścinającego i uwzględniały uproszczone pole radiacji.

Przedstawione badania wskazują na istotność znajomości modelu prędkości podczas rozwiązywania MT oraz wskazują cechy modelu, które mogą powodować błędy, takie jak występowanie wstrząsu na granicy warstw lub obecność warstw o niskiej prędkości. Sieci Lai Chau i Song Tranh zapewniają stabilne rozwiązania MT, natomiast sieci kopalni Rudna i Bogdanka nie powinny być wykorzystywane do rutynowej inwersji MT bez szeroko zakrojonych testów zmienności, jak pokazano w tej pracy, lub informacji *in situ* o efektach w wyrobisku. Zaproponowana metoda implementacji dodatkowych danych HR-GNSS wskazuje na użyteczność w przypadku rejestracji w bliskiej odległości wstrząsów powyżej M=3.5. Pozwala to na poprawę pokrycia azymutalnego. Badania nad wpływem pola pośredniego wskazują na istotność tego problemu i konieczność dalszych badań w temacie. W przypadku stacji sejsmicznych położonych bliżej niż 10 km od źródła warto wziąć pod uwagę wpływ pola pośredniego. Obie zaprezentowane metody mogą wspierać otrzymywanie dobrej jakości rozwiązań MT dla płytkich zjawisk sejsmicznych obserwowanych w bliskich odległościach, np. w monitoringu wstrząsów wywoływanych przez górnictwo podziemne.

Table of contents

1. Introduction 2
2. Methodology 8
   2.1. Seismic moment tensor in modern seismology 8
   2.2. Methods of calculating seismic moment tensor 10
   2.3. First amplitude onset inversion 11
   2.4. Noise bootstrap synthetic tests 14
   2.5. Intermediate field 15
   2.6. Characteristics of research areas 17
3. Results 23
   3.1. Synthetic tests of noise bootstrap 23
      3.1.1. Legnica-Głogów Cooper District (LGCD) 25
      3.1.2. Bogdanka Coal mine 29
      3.1.3. Song Tranh 2 reservoir 32
      3.1.4. Lai Chau reservoir 35
   3.2. High-rate GNSS data in MT 38
   3.3. Intermediate field assumption 44
4. Discussion 50
5. Conclusions 56

References 59

List of figures 65

1. Introduction

When an earthquake occurs, we can register vibrations on the surface, but we do not know the underlying mechanism of its occurrence. Understanding earthquake mechanisms is key to determining their causes, which vary widely. Knowledge of the mechanisms and forces acting deep within the Earth provides vital information about the state of the Earth's crust and the processes occurring there, enhancing understanding of our planet. By analysing earthquake mechanisms, we can infer stresses, strength limits, and stability of the rock mass, enabling the estimation of the geomechanical properties of rocks. Since it is impossible to observe tremor mechanisms directly, conclusions must be drawn from surface-recorded data. It is crucial to identify factors that might lead to seemingly correct but inaccurate solutions and to develop methods for accurately determining earthquake mechanisms.

To discover the mechanism of the earthquake and define the forces acting at the focus, the seismic moment tensor (MT) is commonly determined. The MT is a mathematical way to describe the event mechanism and is a symmetric matrix of 9 components in which each element describes one of the possible pairs of forces acting at the source. The MT solution provides information on potential fault planes and components. The decomposition of the tensor into components allows for a physical interpretation of the mechanism, which is crucial for understanding seismic processes. In addition, it is possible to link the seismic moment tensor with other tremor parameters. MT is routinely determined for large phenomena, e.g. the Global CMT catalogue covering phenomena above magnitude M=5 since 1976 (Dziewoński et al., 1981; Ekström et al., 2012)

The seismic moment tensor is a widely used tool. It is extremely important to identify the limits of applicability and reliability of the method, which is the basis for analysing the situation, especially in places where human life may be in danger. It is necessary to determine what factors may cause incorrect MT inversion results and how they influence them. The work aims to determine the limits of the first P-wave amplitude inversion method and to identify the possibilities of improving the quality of seismic moment tensor inversion solutions using data from high-frequency GNSS records and to determine the correctness of using the far-field assumption. This research hypothesis that the implementation of high-frequency GNSS data and the inclusion of intermediate field terms affect the quality of seismic moment tensor inversion solutions.

Like many methods, seismic moment tensor inversion was originally developed for strong natural earthquakes, i.e. tremors occurring on faults. The expected mechanism for an event on the fault is the double-couple (DC) mechanism, based on shearing movement. Calculating MT can therefore be limited to matching the best DC solution. The exceptions are volcanic tremors, where magma expanding the fissures causes the occurrence of non-shearing components. However, non-shearing components resulting from the overlapping of two DC mechanisms were observed (Frohlich, 1995) . With the development of recording methods and processing seismic parameters, increasingly weaker events were analysed and MT inversion was used for them, including induced or triggered tremors. The earliest studies indicated a similar nature of induced tremors to natural ones, so the same processing methods were used. During the research, other non-shearing sources of events were observed, e.g. in mines. Roof collapse or pillar bursts were indicated by Hasegawa et al. (1989) as typical mechanisms in mines. Due to the presence of non-shear components in anthropogenic tremors, a full tensor solution is usually calculated, contrary to the DC solution in the case of faults. Another difference is that mine tremors occur shallowly and are weaker than natural earthquakes. This means that assumptions true for calculating MT for natural earthquakes may be inappropriate for tensor inversion for anthropogenic events.

Non-shearing components of the seismic moment tensor for natural earthquakes could result from recorded noise, multiple reflections of seismic waves from medium layers, an inaccurate medium model, or errors in the inversion (Kravanja et al., 2002; Kuge & Lay, 1994; Šílený & Vavrycuk, 2000). Non-DC components were used also for anisotropy research (Vavryčuk, 2004). The occurrence of the CLVD component was therefore an indicator of the quality of the mechanism solution when analysing the event on the fault. In the case of induced tremors, the mechanism assumes the participation of non-DC components in the source. For this reason, the seismic moment tensor, and in particular its components, are used as one of the factors to determine whether an event is natural or induced (Cesca et al., 2013). Other case are triggered events which occur on existing discontinuities and mechanism can be mostly shearing.

The recorded waveforms depend on the characteristics of the source, the response of the medium and the response of the instrument. Over the years, many source models have been used for seismic moment tensor inversion, most often assuming a point source with a Dirac-delta source time function. Adopting a specific and simpler model with fewer parameters allows to avoid errors that may result from inversion when general assumptions are used with poor data quality. However, this carries the risk of an incorrect solution if an adopted model is inadequate for the actual earthquake mechanism.

The wrong Green's function resulting from an inaccurate or incorrect velocity model is an important factor in determining the non-shear components of the tensor (Šílený, 2004, 2009). Cases have been observed when the explosive component was omitted in the MT solution due to an inaccurate medium model (Šílený & Hofstetter, 2002). However, the exact model features that influence the inversion have not been determined. For natural earthquakes where body wave frequencies are low, an approximate velocity model is sufficient. Due to the higher frequencies of anthropogenic tremors, the resolution of the velocity model must be higher, as the shorter wavelengths have a greater ability to distinguish details of the medium they propagate. Another problem may be the constantly changing layout of the industry activity area e.g. mine, where the wave propagation is influenced by excavated voids and stress state change dynamically. An inaccurate velocity model will result in a large discrepancy between the recorded and synthetic waveforms. Unfortunately, with a detailed model, location uncertainty will result in the possibility of large changes in modelling the seismic waveform.

The geometry of the seismic network also has a significant impact on the quality of the MT solution. Optimizing network geometry for solving mechanisms was addressed by Ren et al. (2022). A minimum of 5 stations with good azimuthal coverage has been indicated as crucial to obtaining a reliable nodal plane solution (Jechumtálová & Šílený, 2005)). Both the network geometry and the velocity model will affect the quality of the azimuthal coverage. In real conditions, it is not always possible to set the instruments optimally, making it essential to test and evaluate existing networks. Some synthetic studies for the non-DC components were conducted, but the network geometry did not include stations closer than 15 km to the epicentre, which is crucial for small local networks, and the tests were based on a strong natural event with a magnitude of 7.4 (Stierle et al., 2014). Detailed synthetic tests for small events and local network conditions are necessary.

Azimuthal coverage indicated as crucial for MT inversion will depend mainly on the station's orientation concerning the epicentre, the availability of good quality data and the wave path in the medium. A small amount of data is common for weak events. The possibility of using additional data to improve the azimuthal coverage would increase the accuracy of the seismic moment tensor inversion. One of the sciences which support seismology in many fields is geodesy. Measurements by Global Navigation Satellite Systems are used in seismology for strong earthquakes and support early warning systems, e.g. in the field of fast magnitude estimation (Gao et al., 2021; Wei et al., 2022). As proven by Kudłacik et al. (2021) it is possible to register and use records of tremors weaker than M=4 at distances of 7-8 km from the source after specific data processing. The use of an independent data source from seismic network records in the MT inversion could be a valuable method.

It has been proven that the implementation of the first entry of the S wave improves the quality of solutions, including non-DC components (Lizurek et al., 2021; Stierle et al., 2014; Teyssoneyre et al., 2002). However, seismic records from areas of anthropogenic seismicity may be noisy or the geological structure may not allow for a certain determination of the first entry of the S wave, which can be observed in the Legnica-Głogów Cooper District area (Kokowski & Rudziński, 2023). Additionally, the energy of the non-shear components is carried mostly by the P wave (Fletcher & McGarr, 2005). Surface waves were also used for tensor inversion (Toksöz & Kehrer, 1972)), but due to the short event-station distances, they may not be registered in local networks (Gibowicz & Kijko, 1994). For this reason, it is necessary to develop methods that will increase the reliability of MT solutions without using S waves.

Many seismological methods assume that observations are made in the far-field (Aki & Richards, 2002). This assumption allows for simplification and enhancement of calculations. However, when the far-field assumption is incorrect, an error is introduced to the calculations. The far-field assumption is fulfilled when the distance from the source is several wavelengths, so it is frequency dependent. The near-field is often defined in terms of permanent displacement, and since anthropogenic tremors are characterized by small sources, the chance of registration in the near-field is small. However, it is worth investigating the effect of the intermediate field term, as its impact does not decrease with distance as quickly as the effect of the near-field.

Inversion methods are used to determine MT in both the time and frequency domains. These methods are based on the inversion of amplitudes, their ratios or full waveforms. Full waveform inversion is widely applied for natural earthquakes, however for anthropogenic tremors is not so convenient as waveforms reflect detailed structure and careful preprocessing is demanded. Other methods provide nodal planes solutions based on the first onset polarities, but without moment tensor. A simple MT inversion method is the first P-wave onset. As a simple method, it has a small amount of input that allows for the analysis of the influence of individual factors. Additionally, the first P-wave amplitude inversion is commonly used to analyse weak induced events or microearthquakes (Vavryčuk et al., 2017).

The commonly used method of induced seismic events MT calculations need to be examined for sensibility for a wide range of factors. Relevant to correct MT solution are azimuthal coverage and noise, but the distinct influence on MT solution is undetermined. Knowledge about possible errors will allow us to improve MT solutions interpretation. Methods other than S waves onset implementation should be developed. Especially methods that improves focal coverage will be valuable. Additionally, often applied assumptions, like a far-field, should be examined if are fulfilled

As the first stage of the research, synthetic tests were carried out, where synthetic amplitudes were generated based on the assumed mechanism, and after adding noise, the mechanism was solved. The tests were carried out for four seismic networks established for anthropogenic seismicity monitoring: Legnica-Głogów Cooper District, Bogdanka mine, Song Tranh 2 reservoir and Lai Chau reservoir. Different mechanisms were analysed, from shear to non-DC under noise levels up to 40%. To eliminate errors related to determining the depth of the event in synthetic research, a set of depths was analysed, which included the ranges in which tremors are located in the four considered areas. The impact of the velocity model on the solution quality was determined.

As the first way to improve MT inversion, the possibility of implementing high-rate (HR) GNSS data to increase the azimuth coverage was checked. The analysed data concerned two seismic events with magnitudes M=3.8 and M=4 occurring in the LGCD area. The quality of the solutions was checked when implementing this data into the MT tensor inversion using the spectral level.

The last stage was to determine the influence of the intermediate field on the amplitudes recorded at stations at different distances from the source based on the networks in LGCD and

Song Tranh. The research was based on the assumption of the Haskell model for a shear source and took into account a simplified radiation pattern.

The presented research focuses on the reliability of MT inversion of non-DC earthquakes, possibilities of application HR-GNSS in MT inversion and intermediate field influence on registered amplitudes. The following chapters will discuss methodology, results and analysis in detail.

2. Methodology

2.1. Seismic moment tensor in modern seismology

The seismic moment tensor is the description of forces acting in an earthquake source in the form of nine element matrix. The earthquake mechanism can be described by a couple of forces acting in the earthquake source. If the force couple acting in opposite directions and the force's arms are shifted the moment of force appears. Due to the law of conservation of angular momentum, the perpendicular force couple appears (Aki & Richards, 2002). The double couple mechanism represents the shearing mechanism on a fault. The shearing movement forces in earthquake source can cause other mechanisms if occurred simultaneously in different directions, such as volume changes or crack opening. Regardless of the source mechanism the seismic waves in a low frequency range from the seismic point source are radiated and the displacement on the surface follows the equation (Aki & Richards, 2002):

$$u_i(x,t) = \frac{dG_{ij}(x,t;x_0,t_0)}{d(x_0)_k} * M_{jk}(x_0,t_0) = G_{ij} * M_{ij}. \qquad (1)$$

where $M_{jk}(x_0,t_0)$ is the seismic moment tensor as a set of nine force couples, and G_{ij} is the Green function. The Green function describes the rock medium response to the delta pulse force in seismic source on a distance between the source and receiver.

Mathematically the moment tensor (MT) is a nine-element matrix M_{ij} describing nine possible directions of force couples and arms acting in an earthquake source (Gibowicz & Kijko, 1994). MT is a square, symmetrical matrix, with six independent components, where *i* is the force acting direction and j is the force arm direction which causes the moment. Matrix elements located along the diagonal describe the isotropic part of the seismic mechanism. The other elements are complementary force couples. This feature gives the possibility of tensor decomposition into isotropic component tr(M)=M11+M22+M33 and deviatoric part M'. Diagonalization of the matrix M' allows for further decomposition and extraction of the double couple component.

The most popular decomposition of seismic moment tensor gives us a double couple (DC) component for pure shear, a CLVD for uniaxial compression or tension, and an isotropic component for volume changes (Jost & Herrmann, 1989). Such decomposition is used because of its usefulness for physical interpretation (Baker & Young, 1997; Cesca et al., 2013; Fletcher & McGarr, 2005;

Rudzinski et al., 2016; Vavryčuk, 2015). There is also a decomposition method with the isotropic and major and minor double couple described by e.g. Wallace (1985). Other decomposition indicates isotropic components and the mixed mode tensile crack as a general dislocation crack model (Vavryčuk, 2001).

Except for the information about the components, moment tensor inversion allows the determination of possible fault planes and stress axes. The tension and compression quadrants can be distinguished based on the polarity of the first P-wave amplitude. Two perpendicular planes separating these areas are determined and called nodal planes. Each nodal plane is potentially the fault plane, but without additional information, the exact one cannot be determined (Gibowicz & Kijko, 1994).

The focal mechanism can be represented in graphical form on the focal sphere, which is called a beach ball. Nodal planes, tension and compression axis and quadrants, and the receivers can be projected on the hemisphere. Such representation allows for easy determination of fault orientation and main forces directions.

For comparison of many mechanisms or quick mechanism components valuation, the source plots in diamond shape are used. The vertical axis of such a plot is the isotropic axis, while the horizontal one is the CLVD axis. The pure DC mechanisms are placed on the axis intersection point. Figure 1 presents a source-type plot proposed by Hudson et al. (1989) with mechanisms with different DC components.

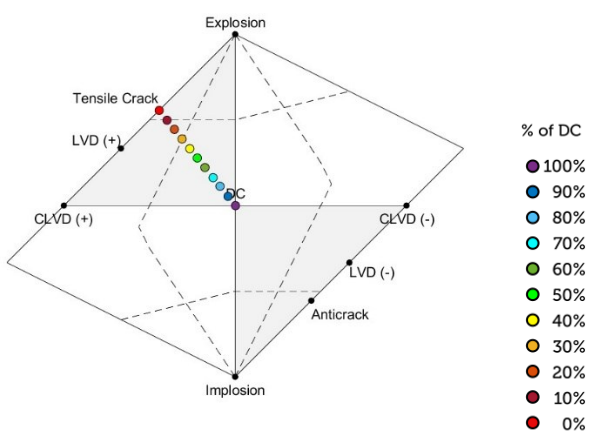

Figure 1 Source-type diamond plot with mechanisms with DC component decreasing by 10%. The Violet dot is a pure shearing mechanism, when red one is for a pure tensile crack with no DC component.

2.2. Methods of calculating seismic moment tensor

Focal mechanisms are researched by moment tensor inversion. For all MT inversion methods, the quality of a data set is significant. A high signal-to-noise ratio is necessary as well as good coverage of the focal sphere (Šílený et al., 1996). The low band-pass filter is commonly used for high frequency noise elimination. Linear trends and instrument influence have to be removed, also rotation of the waveforms into radial and transverse coordination system could be done (Gibowicz & Kijko, 1994). As the polarization of the registered waveforms is used for the nodal planes and the tension-compression quadrants determination it is important to verify the instrument polarization. Furthermore, the proper calculation of Green's function is complicated for simple Earth models, so for heterogenic conditions reliable Green's function becomes even more challenging. The assumptions that have to be fulfilled as a far-field term, point source, and pulse source time function increase the possibility of miscalculating the moment tensor.

Besides the challenges of the MT calculations, a wide range of moment tensor inversion methods were developed. These methods can be divided into time domain methods and frequency domain methods. Apart from the applied domain, the displacement can be presented in a matrix form as:

$$u=Gm \qquad (2)$$

In the time domain the G is nx6 matrix of the Green functions calculated for specific n stations, m is a six-element vector of the independent moment tensor elements, and u is a vector of the measured displacements. For frequency domain problem contains a series of equations, each for a separate frequency, U is the displacement spectra; m contains additionally the source time function transform for moment tensor elements. All terms on the equation in the frequency domain are described by the real and imaginary parts. As the above equation presents the linear dependence usually the last-square problem approach is applied.

For strong events recorded at regional distances, the full waveform inversion is widely applied (Cesca et al., 2006; Dziewonski et al., 1981; Sipkin, 1982). This method is not so convenient for the weak, e.g. anthropogenic events where high frequencies reflect the detailed structure of a rockmass in registered waveforms. This feature implicates the more complex Green's function with more probable mistakes during its computations. An additional disadvantage of full waveform inversion is the need for careful preprocessing of data, which makes employing such methods in everyday usage challenging. Other possible methods use amplitude ratios (Hardebeck & Shearer, 2002) or surface waves (Toksöz & Kehrer, 1972). Surface waves however should not be recorded by local seismic networks in short distances, e.g. in underground mining induced events (Gibowicz & Kijko, 1994). Methods using amplitude ratio are mainly limited by the necessity of noise level determination (Hardebeck & Shearer, 2002). There are relative moment tensor determination methods where the need for Green's function computation is removed. However, the reference mechanism is needed, and the method applies to earthquake clusters (Dahm & Brandsdóttir, 1997). Another method for events clusters is Hybrid MT, with the possibility to provide station correction factors (Kwiatek et al., 2016). The Bayesian approach for moment tensor inversion is also applied in some cases, however requires knowledge about input parameter errors and gives high uncertainty for non-DC components (Gu et al., 2018). The simple method of MT calculation is to use amplitudes of seismic body waves, for example, the first P-wave ground-displacement pulse (Kwiatek et al., 2016). The P-wave MT inversion advantages are easy and little demanding computations.

As previous research shows (Rudzinski et al., 2016) method used for MT inversion influences the solution, especially for events with complex rupture. The method selected for MT inversion depends on available data and a priori knowledge however, different methods can provide different MT solutions. For the study about an event from 19 March 2019 in Rudna Mine MT was resolved for three sets of data with three different methods: in-mine recordings with first onset amplitude inversion, local surface data with full waveform inversion, and regional data with amplitude spectra fitting. Each method gives another solution and another information about the stages of rupture history.

For the inversion of the seismic moment tensor, various methods have been developed. The use of a specific method will depend on the data quality, character of an event, and availability of additional information. The use of each method is associated with certain limitations.

2.3. First amplitude onset inversion

The first amplitude onset inversion method is used for small events and is recommended for anthropogenic events (Vavryčuk et al., 2017). As the method is based on the first peak of the P-wave the noise-to-signal ratio is crucial. In the first P-wave amplitude inversion MT is calculated by resolving a set of linear equations (2) (Kwiatek et al., 2016). For simplifying the far-field term is usually considered in MT calculations when the near and intermediate field term is ignored. The impulsive point source is also assumed. The system of equations is overdetermined and is typically resolved with the use of L2 norm. The optimum MT solution gives the minimum root mean square error defined as an absolute difference between synthetic and measured displacement amplitudes (Kwiatek et al., 2016):

$$RMS = \sqrt{\frac{\sum_{i=1}^{N}\left(U_i^{measured} - U_i^{theorethical}\right)^2}{\sum_{i=1}^{N}\left(U_i^{theorethical}\right)^2}} \tag{3}$$

For described research hybrid MT package (Kwiatek et al., 2016) was used. The calculations are based on the omega parameter considered as the integral of the first ground displacement pulse or the displacement spectral level of the P-wave also called spectral amplitude. A sign of the amplitude is applied to determine tension and compression quadrants, so the positive sign means ground movement from the source, and the negative means movement toward the source. The omega parameter for simplification is calculated as the triangle area based on amplitude and pulse duration information.

Two types of input files were used for calculations in the Hybrid MT package depending on the available information. Both contained information about the station name, component, seismic phase, velocity and density of the rocks in a source, and omega parameters. The first type of file used azimuth, source-station distance, incidence angle, and takeoff angle values as defined in Figure 2. The second type of file contains station coordinates, and necessary parameters are calculated by the built-in function. Moment tensor inversion was performed with the L2 norm and the graphical representation was on the lower hemisphere with the Schmidt projection. As a result, the full, deviatoric, and double couple solutions were given. For all types of results six independent elements of moment tensor were calculated with RMS error and covariance matrix, isotropic, CLVD and DC components, scalar seismic moment with moment magnitude and nodal planes and stress axis directions. Information about theoretical amplitudes was also provided.

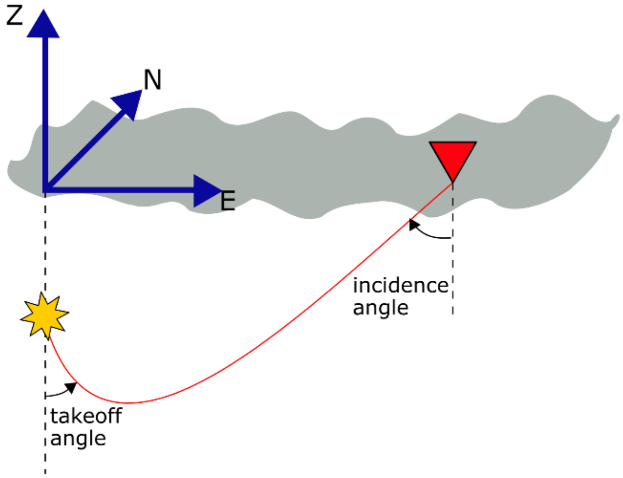

Figure 2 Seismic wave path description with the definitions of incidence and takeoff angles.

The assumed model is a tensile crack earthquake. The slip on a fault then is described by the tensile angle calculated from the fault plane toward the slip vector. The angle value is 0° for pure shearing mechanism, 90° inclination for crack opening and – 90° for crack closing. The percentage of isotropic, CLVD and DC components depends on a tensile angle as shown in Figure 3. The tensile angle was used for modelling complex non-shearing mechanisms (Vavryčuk, 2001).

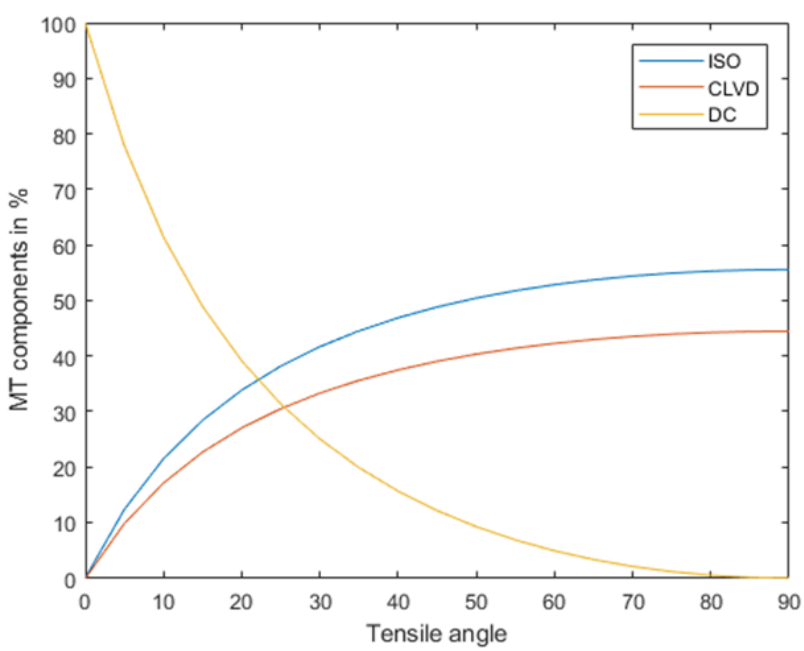

Figure 3 The moment tensor ISO, CLVD and DC components participation in full solution depending on the tensile angle.

2.4. Noise bootstrap synthetic tests

The additional capabilities of Hybrid MT software were used to evaluate the reliability of results. Except for the RMS error, Jackknife station rejection tests were performed to determine stations crucial for exact seismic network geometry. The disturbance of amplitude value, amplitude polarization, and takeoff value can be added to assess the stability of solutions or to identify conditions with a high risk of instability. In this research, mostly amplitude values were changed to imitate noise influence on synthetic amplitudes.

The amplitude disturbance is added to all amplitudes and the amplitude value is modified with the equation

$$u_i = u_i + x \cdot u_i \cdot \frac{N(0,1)}{3.0} \tag{4}$$

where u_i is the measured amplitude, N(0,1) is the random value with mean 0 and standard deviation 1 drawn from normal distribution and x is a declared factor (Kwiatek et al., 2016).

The primary aim of conducting synthetic tests was to verify the reliability of moment tensor solutions for non-double-couple (non-DC) mechanisms by comparing assumed mechanisms with the resulting mechanism across different depths, mechanisms, and varying levels of noise contamination. Initially, synthetic amplitudes and polarities were generated. The Hybrid MT software facilitated the generation of initial peak amplitudes for specific event parameters: location, magnitude M_W, depth, fault plane strike, dip and rake, 1D velocity model, and tensile angle (Kwiatek et al., 2016). Various tensile angles were examined, ultimately selecting values where the assumed DC component decreased by 10%. Velocity models for the area were sourced from the EPISODES platform (Orlecka-Sikora et al., 2020). Subsequently, synthetic amplitudes were utilized to compute moment tensors for four noise levels. In practical MT inversion applications, data from all stations may not always be available, so to ascertain the significance of each station in a network for stable MT solutions, Jackknife station rejection tests were performed. In each iteration, one station was omitted to evaluate the quality of the MT solution with an incomplete dataset. Synthetic Gaussian noise was added at levels averaging 10%, 20%, 30%, and 40% of the generated amplitudes. Each noise bootstrap test was repeated 100 times.

To determine if the examined MT solution both synthetic tests and real cases is reliable four characteristics were taken into account besides RMS values: calculated components (ISO, CLVD, and DC percentage), the accordance of ISO and CLVD components sign, fault type accordance with the assumed one and stability of solutions as comparison of the nodal planes or P, T axes directions for full, deviatoric and DC solutions.

The stability of the MT inversion solution was determined with the use of rotation angle calculation. The rotation angle is defined as the smallest possible rotation between two sets of axes or nodal planes (Kagan, 1991). This allows for comparing MT with the reference solution. The stable solution was assumed for results with a rotation angle smaller than 10°.

2.5. Intermediate field

The displacement u in place x and time t is defined as (Aki & Richards, 2002):

$$u(x,t) = \frac{1}{4\pi\rho}\frac{1}{r^4}R^N\int_{r/\alpha}^{r/\beta}\tau M_0(t-\tau)d\tau + \frac{1}{4\pi\rho\alpha^2}\frac{1}{r^2}R^{IP}M_0(t-r/\alpha) + \frac{1}{4\pi\rho\beta^2}\frac{1}{r^2}R^{IS}M_0(t-r/\beta) + \frac{1}{4\pi\rho\alpha^3}\frac{1}{r}R^{FP}\dot{M}_0(t-r/\alpha) + \frac{1}{4\pi\rho\beta^3}\frac{1}{r}R^{FS}\dot{M}_0(t-r/\beta) \quad (5)$$

where M_0 is a scalar seismic moment, R are radiation patterns for near (N), intermediate (I) and far (F) fields for P- or S-wave, α and β are velocities of P and S-wave, respectively, r is source-receiver distance, and ρ is the rock density in foci. The above equation describes the displacement caused by the double-couple source. Usually, the assumption in MT inversion calculations is that all stations are in a far-field. This part focuses on the influence of intermediate field term on displacement.

This research is based on a Haskell model with progressive slip along the fault which is uniform for the whole fault surface (Gibowicz & Kijko, 1994). The assumption of the Haskell model is the ramp function describing the linear displacement increase from zero for t<0 to one for t=T called the rise time. This determines the source time function $M_0(t)$ describing the pulse radiated from the fault (Stein & Wysession, 2003), as shown in Figure 4.

As the velocity is the derivative with respect to time it is possible to write the relation between $M_0(t)$ and $\dot{M_0}(t)$ where Δt is the displacement pulse duration.:

$$M_0 = \int_0^t \dot{M}_0\, dt \quad (6)$$

$$M_0 = \dot{M}_0 * \Delta t \quad (7)$$

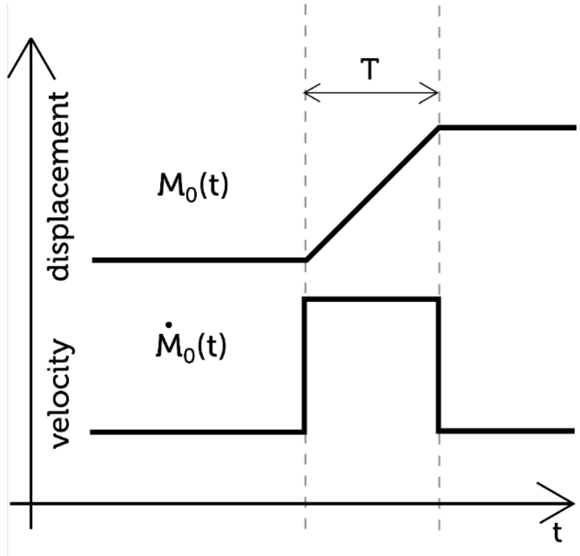

Figure 4 Source time function for Haskell fault model.

Such assumption allows for simplification in the part of the equation (5) responsible for the P-wave intermediate field:

$$u^{IP} = \frac{1}{4\pi\rho\alpha^2}\frac{1}{r^2}R^{IP}\dot{M}_0\Delta t \qquad (8)$$

and from the comparison of the equation part for far-field P-wave:

$$u^{FP} = \frac{1}{4\pi\rho\alpha^3}\frac{1}{r}R^{FP}\dot{M}_0 \qquad (9)$$

the condition to far and intermediate field influence on the measured displacement to be balanced, if we neglect the radiation patterns, is as follows:

$$r = \Delta t * \alpha \qquad (10)$$

The simple conclusion was made that intermediate and far field equal influence on amplitudes influence depends on the duration of the first P-wave peak and P-wave velocity.

The previously neglected radiation patterns can be included easily if reduced by the assumption that seismograms are rotated so the up direction is the vector away from the source. The radiation patterns for P-waves are as follows (Aki & Richards, 2002):

$$R^{IP} = 4\, sin2\theta cos\phi \boldsymbol{R} - 2(cos2\theta\cos\theta\, \boldsymbol{\Theta} - \cos\theta\sin\phi\boldsymbol{\Phi}) \qquad (11)$$

$$R^{FP} = sin2\theta cos\phi \boldsymbol{R} \qquad (12)$$

Where R, θ, Φ are vectors in three directions. Parts of equations with R are the radial components, while the remaining part of the equation for an intermediate field is the transverse component. Because we are interested only in records that were rotated the transverse part can be neglected. The simple relation can be derived:

$$R^{IP} = 4R^{FP} \qquad (13)$$

2.6. Characteristics of research areas

This research uses data from four cases of anthropogenic seismicity. Two of them are underground mines placed in Poland, and the other two are artificial reservoirs in Vietnam. All places are monitored by the local surface seismic networks equipped with triaxial seismometers. Detailed information about sensors, locations, and operating times can be found on the EPISODES platform (Orlecka-Sikora et al., 2020).

The LUMINEOS network is a surface seismic network established to monitor seismic activity within the Rudna copper mine located in southwest Poland, specifically in the Legnica-Głogów Copper District (LGCD). Within the Rudna mine, an ore is extracted using a chamber-pillar system at depths ranging from 600 m to 900 m. The geological structure of the area is relatively simple without large discontinuities, characterized by overlaying strata and layers that dip slightly towards the northeast (Figure 5). Beneath the excavation levels, there exists a low-velocity anhydrite layer. Seismic activity in this region is primarily induced by mining activities and is closely linked to the rate and extent of exploitation (Kozłowska, 2013). Events are located usually in the vicinity of the excavation level on depths 600m- 1200 m. The seismic network contained from 6 up to 17 sensors, depending on the period (Figure 6b). The mean distance between stations is less than 6 km. Except for the short-period seismometers Lennartz 3D Lite (1 s) or Geosig VE-53-BB (5 s-160 Hz), also GeoSIG AC-73 accelerometers were established for ground motion monitoring. Annually, more than 1000 events with magnitudes exceeding M>1 are recorded in this area, rendering LGCD the most seismically active region in Poland, including strong and tragic events (e.g. (Lizurek et al., 2015; Rudzinski et al., 2016)).The strongest event occurred in LGCD was M_w=4 The mechanisms of these tremors are largely associated with mining operations, with predominantly non-shearing characteristics observed (Lizurek et al., 2015; Lizurek & Wiejacz, 2011; Rudzinski et al., 2016). Seismic data from this network are accessible on the Episodes Platform (IS-EPOS, 2017).

A network of seismic stations, named BOIS (BOgdanka mine Induced Seismicity), has been established to monitor underground tremors at the Bogdanka coal mine in eastern Poland's Lublin Mining District. The network comprises 12 stations with broadband seismometers (GeoSIG VE-53/BB) positioned between 2 km and 16 km apart from each other (Figure 6a). The Bogdanka mine extracts coal deposits located at depths ranging from 500 meters to 1200 meters. The longwall mining system is employed, which involves creating a cavity behind the working face while leaving narrow pillars of coal (approximately 5 meters wide) for support (Philpott, 2002). The strongest seismic event recorded by the network occurred on October 2, 2021, with a magnitude of M=3.7. On average, the mine experiences more than 10 tremors exceeding M=0.5 each week. Geologically, the area features a simple structure with northwest-dipping strata interrupted only by minor normal faults (Figure 5). Seismic data acquired by the BOIS network is accessible through the Episodes Platform (EPISODES, 2019).

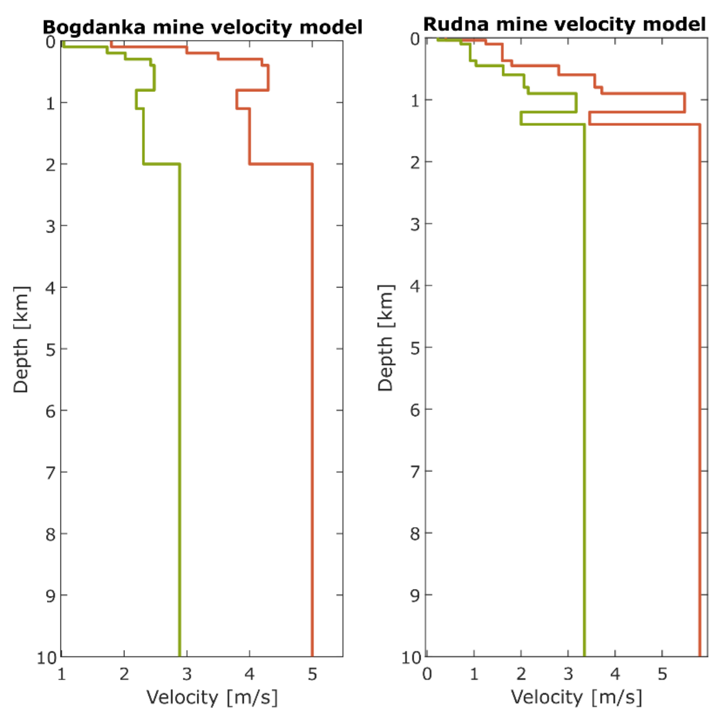

Figure 5 Velocity models for Bogdanka and Rudna mine

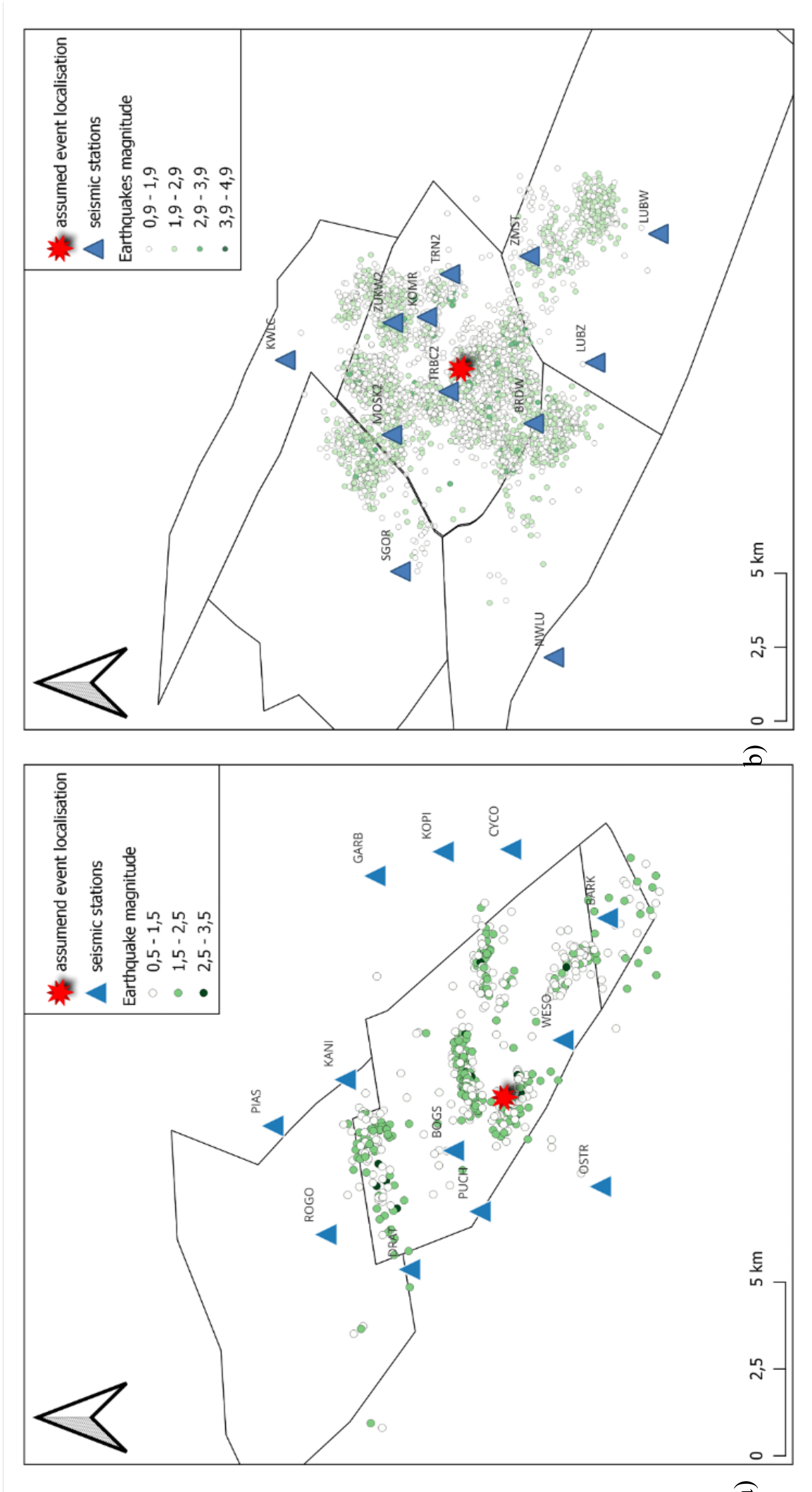

Figure 6 Maps for mine areas with seismicity a) Bogdanka mine, b) LGCD area.

The VERIS (ViEtnam Reservoir Induced Seismicity) network was established to monitor seismic activity induced by the creation of an artificial reservoir. Situated on the Tranh River in central Vietnam, the Song Tranh 2 reservoir area was previously considered aseismic, with only 13 small earthquakes recorded since the XVII century, the strongest of which had a magnitude of M=4.7. Reservoir impoundment began in November 2010, and seismic activity has been observed to increase steadily since 2011 (Wiszniowski et al., 2015). The seismic activity was the rapid response in the beginning phase of reservoir filling, then the regime changed to delayed response in the following time. The reservoir has a capacity of 740 million cubic meters, and the water level changes from 140 m up to 175 m. The seismic network, comprising up to 10 seismometers during peak activity periods was composed of Lennarts LE-3Dlite, GeoSIG VE-53/BB and Guralp CMG-6T/30ST2 broadband triaxial seismometers. Seismic activity in this region exhibits seasonal variations correlated with the wet and dry seasons and the water level of the reservoir (Lizurek et al., 2021). Notable earthquakes in the area include those on September 3, 2012, with a magnitude of M4.2, October 22, 2012, with a magnitude of M4.6, and November 15, 2012, with a magnitude of M4.7. These events are often located close to and beneath the reservoir, occasionally occurring along existing fault lines (Figure 8b). Focal mechanisms obtained from these events typically indicate normal faults with a predominance of shearing components despite of strike-slip tectonic regime (refer to Figure 1 and Figure 9 in Lizurek et al. (2017)). Further details on the seismic activity of the area can be found in recent studies by Gahalaut et al. (2016) and Lizurek et al. (2017). All data, including moment tensor solutions, are accessible on the EPISODES platform (IS-EPOS, 2017).

Established in 2014, the Lai Chau seismic network was designed to monitor seismic activity associated with a newly built reservoir in Vietnam's northern Lai Chau province. The network's development continued in subsequent years, and it currently comprises up to 10 seismic stations equipped with Guralp, STS-2 or GeoSIG triaxial broadband seismometers, spaced between 4 km and 112 km apart. The placement of these stations was heavily limited to areas accessed by existing roads, resulting in limited coverage west of the reservoir (Figure 8a). While the background seismic activity is primarily linked to the Nam Nho-Nam Cuoi and Moung Te fault zones, tremors were also detected near the dam in the eight months preceding impoundment. Reservoir filling began in June 2015 and concluded in July 2016. Interestingly, a decrease in seismic activity was observed immediately following impoundment. However, the network recorded a maximum magnitude event of M_L 5.1 on August 13, 2018 (Lizurek et al., 2019). These events originated at depths ranging from 4 km to 15 km and are located mainly on discontinuities with only a few in close vicinity of the reservoir. Data collected by the Lai Chau network facilitated the calculation of 12 moment tensor solutions using first P-wave amplitude inversion. The derived mechanisms primarily indicated shear-normal and strike-slip faulting. All data, including the MT solutions, are accessible through the EPISODES platform (EPISODES, 2018).

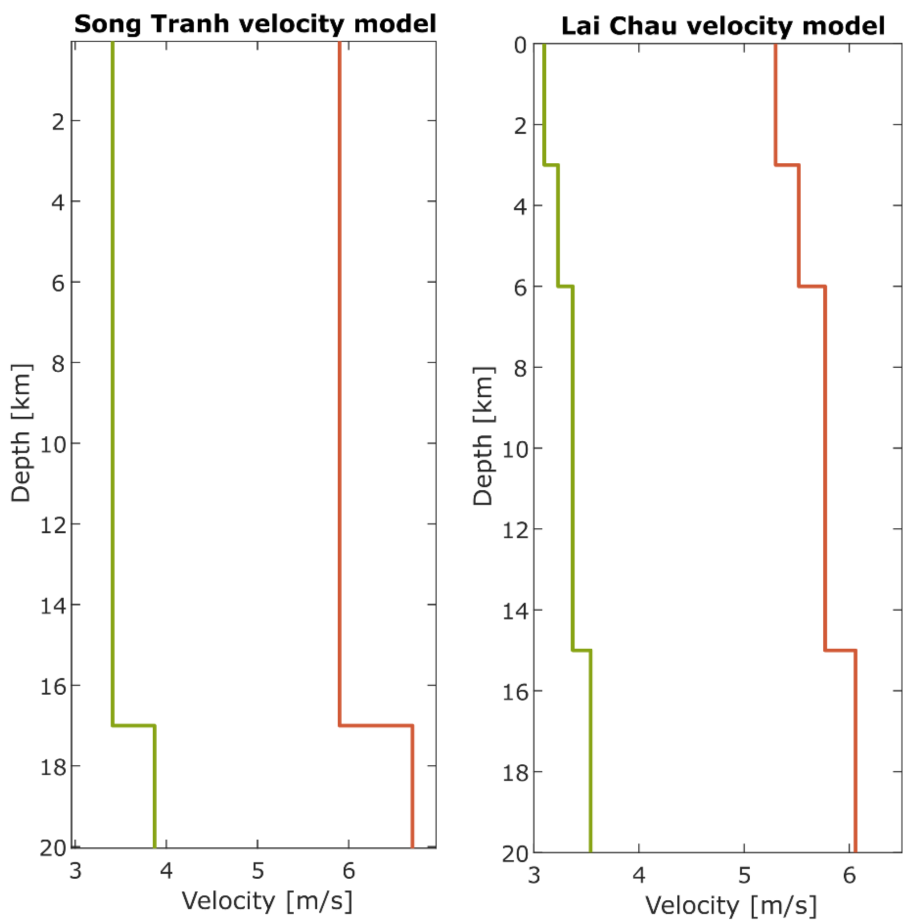

Figure 7 Velocity models for Song Tranh 2 and Lai Chau areas.

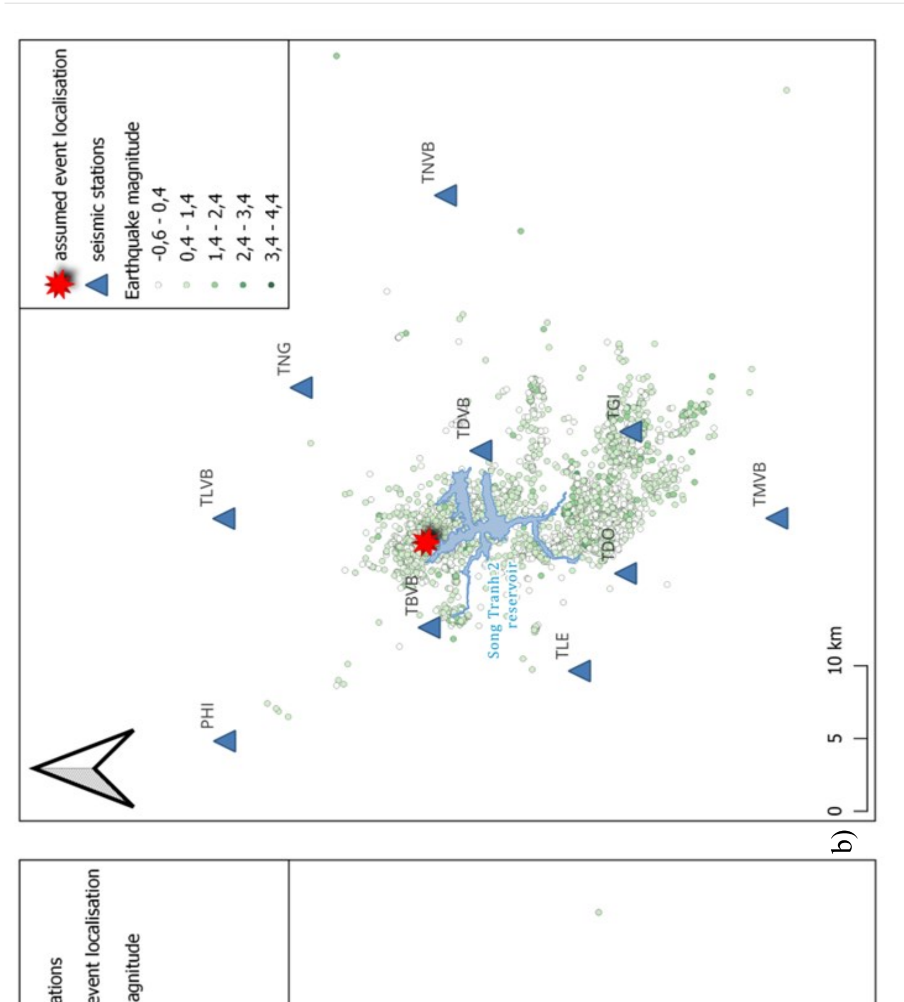

Figure 8 Maps of seismicity for artificial reservoir areas a) Lai Chau, b) Song Tranh.

3. Results

3.1. Synthetic tests of noise bootstrap

The synthetic tests investigate the influence of network geometry, depth, and noise on moment tensor (MT) inversion for induced or triggered seismicity events. Depths ranging from 500 m to 8 km were applied to both mining networks, with additional calculations for artificial reservoir networks at depths of 10 km and 15 km to cover locations of recorded events. This depth range encompasses shallow events recorded in the mining networks and deeper events occurring in the reservoir areas, enabling comparison between the two. As an initial test, the Jackknife single station rejection tests were performed. The Jackknife single station removal test showed minimal impact on solutions for most cases (Figure 9). Only removal of the TRBC station in Legnica-Głogów Copper District, the closest to the event, resulted in a reversed fault type for events shallower than 1 km. This highlights the importance of TRBC for accurate MT inversion due to its proximity and the network's limited focal coverage (Figure 10).

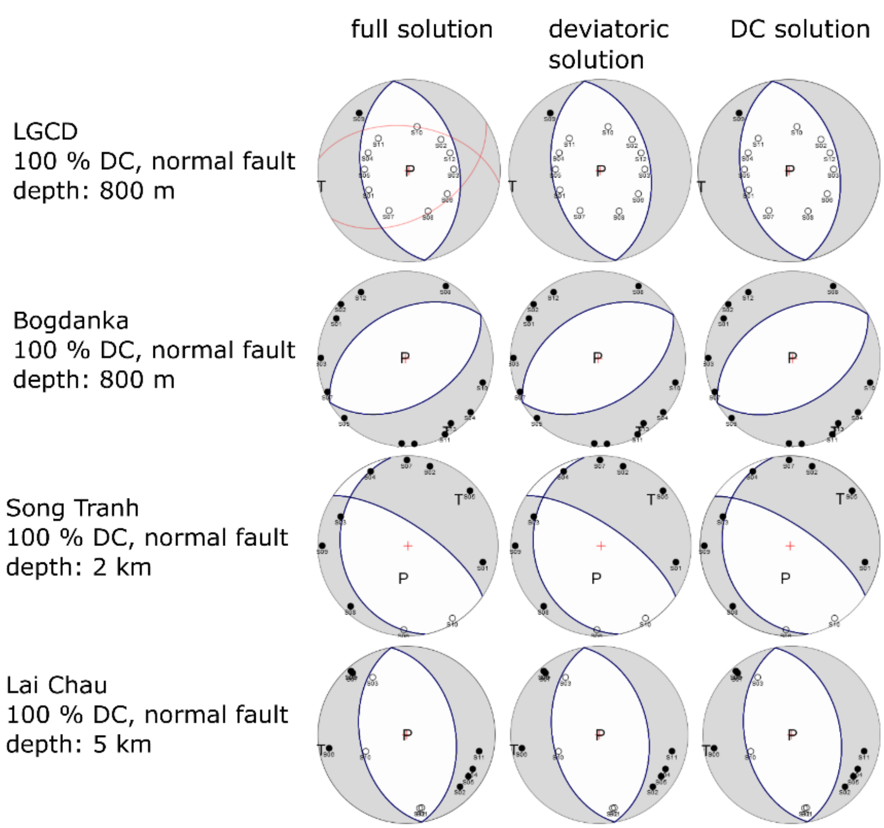

Figure 9 Jackknife single station rejection tests for all networks. Red lines in full solution for LGCD network show the nodal planes of solutions with excluded TRBC station.

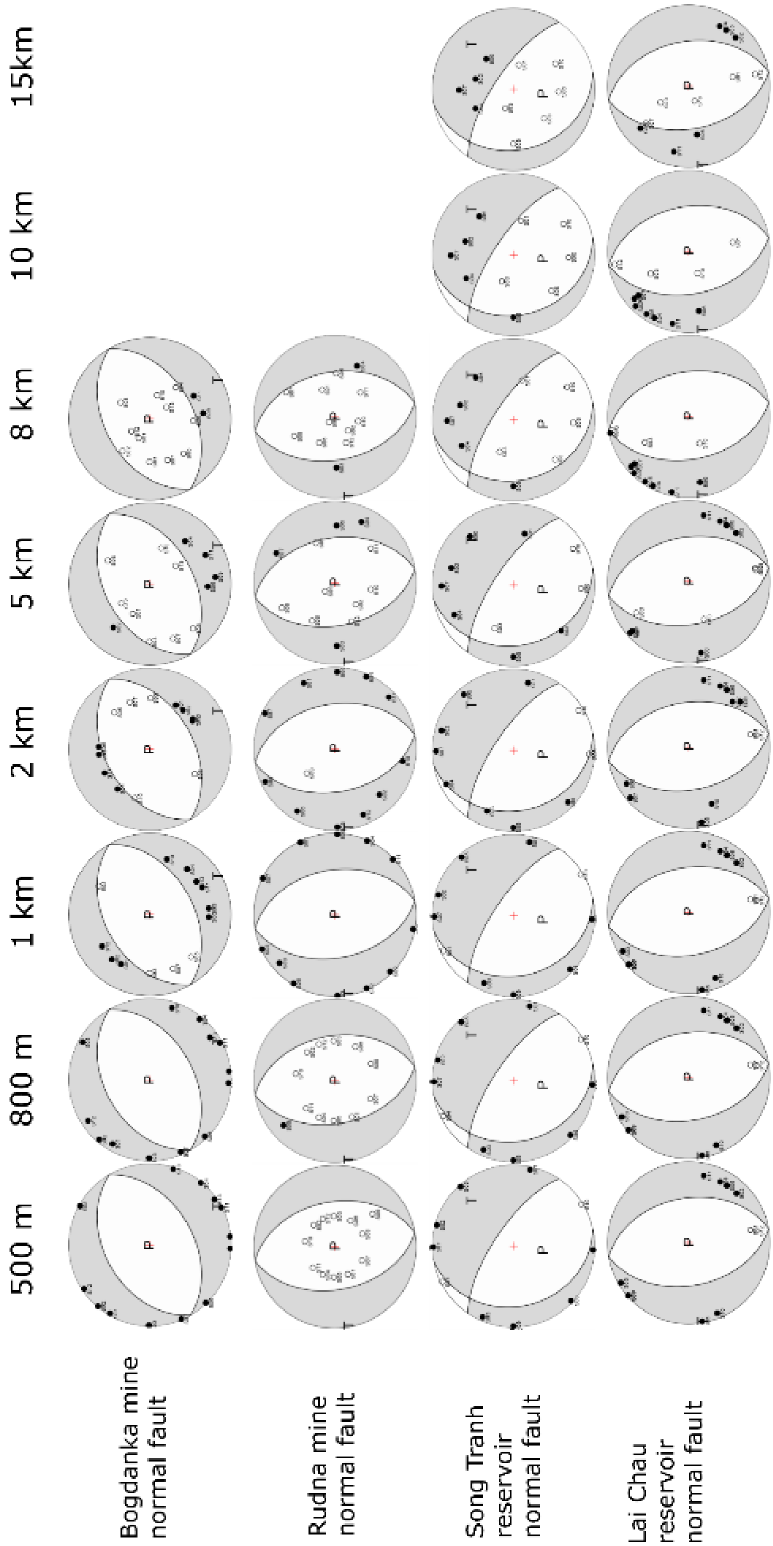

Figure 10 Focal coverage of the MT solution in depth for different networks.

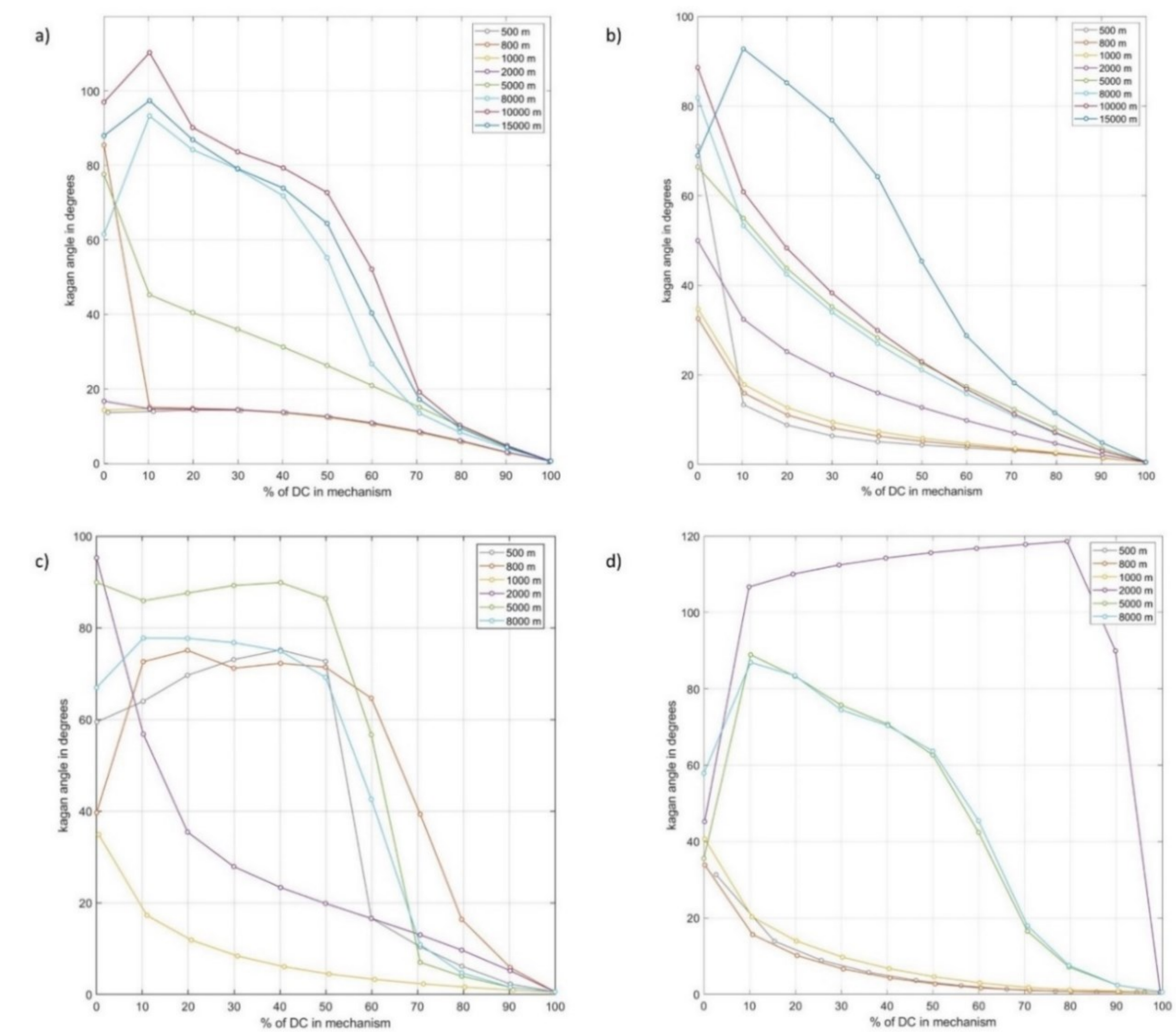

Figure 11 Rotation angle between full and deviatoric solution for a) Song Tranh, b) Lai Chau, c) LGCD, d) Bogdanka mine.

3.1.1. Legnica-Głogów Cooper District (LGCD)

The assumed seismic source for LGCD tests was situated near the TRBC station, in the centre of the network, where one of the strong events occurred. A fault plane with strike/dip/rake of 170°/46°/±90° was used, and a magnitude of M_w=3.7 was applied for all synthetic tests. The focal coverage changes significantly depending on the depth. The cause is a complex velocity model with high gradients. The stability of solutions is also strongly connected with the velocity model (Figure 11c). Despite depth events assumed more than 70% DC had a rotation angle smaller than 40°. The non-shearing mechanisms were stable only for 1 km and 2 km depth events. Low velocities near the surface influence mechanisms on a depth of 500 m, and a boundary layer of 800 m depth makes moment tensor inversion unstable. Deeper events exceeded station-event distance which results in instability of non-DC mechanisms.

In the LGCD noise bootstrap analysis, a noise level of 10% resulted in an RMS value below 0.15 for both fault geometries. With a 20% noise contamination, the RMS did not exceed 0.3 regardless of the type of fault. However, at a 30% noise level, the RMS increased to up to 0.4 for normal fault geometry and 0.5 for reverse fault geometry. At a 40% noise level, the RMS reached up to 0.6, although there were isolated cases exceeding 0.4. Generally, RMS values increased with each increment in the noise level.

In tests conducted for the LUMINEOS network, the MT components were generally well resolved across most depth ranges. Results for normal and reverse fault mechanisms were not diverse (Figure 12, Figure 13). However, for very shallow events at a depth of 500 m, there was significant scattering, and solutions for the double-couple mechanisms exhibited numerous non-physical solutions even for low noise contamination. As depth increased, the MT components were resolved with better consistency with the assumed ones up to 5 km, except for the 1 km depth, where many non-physical solutions were observed. The 1 km noise bootstrap resulted in scattered solutions tending to be divided into two clusters near the tensile crack and anticrack regardless of the type of assumed mechanism. The 8 km depth for noise contamination was resolved worse than more shallow events, although not significantly. A noise level of 40% results in many nonphysical solutions for almost all depths.

The typical depth of events located in the LGCD area varies from 700 m to 900 m. Synthetic tests for 800 m present proper components solutions and low RMS error estimation, without the stability between full, deviatoric and double-couple solutions.

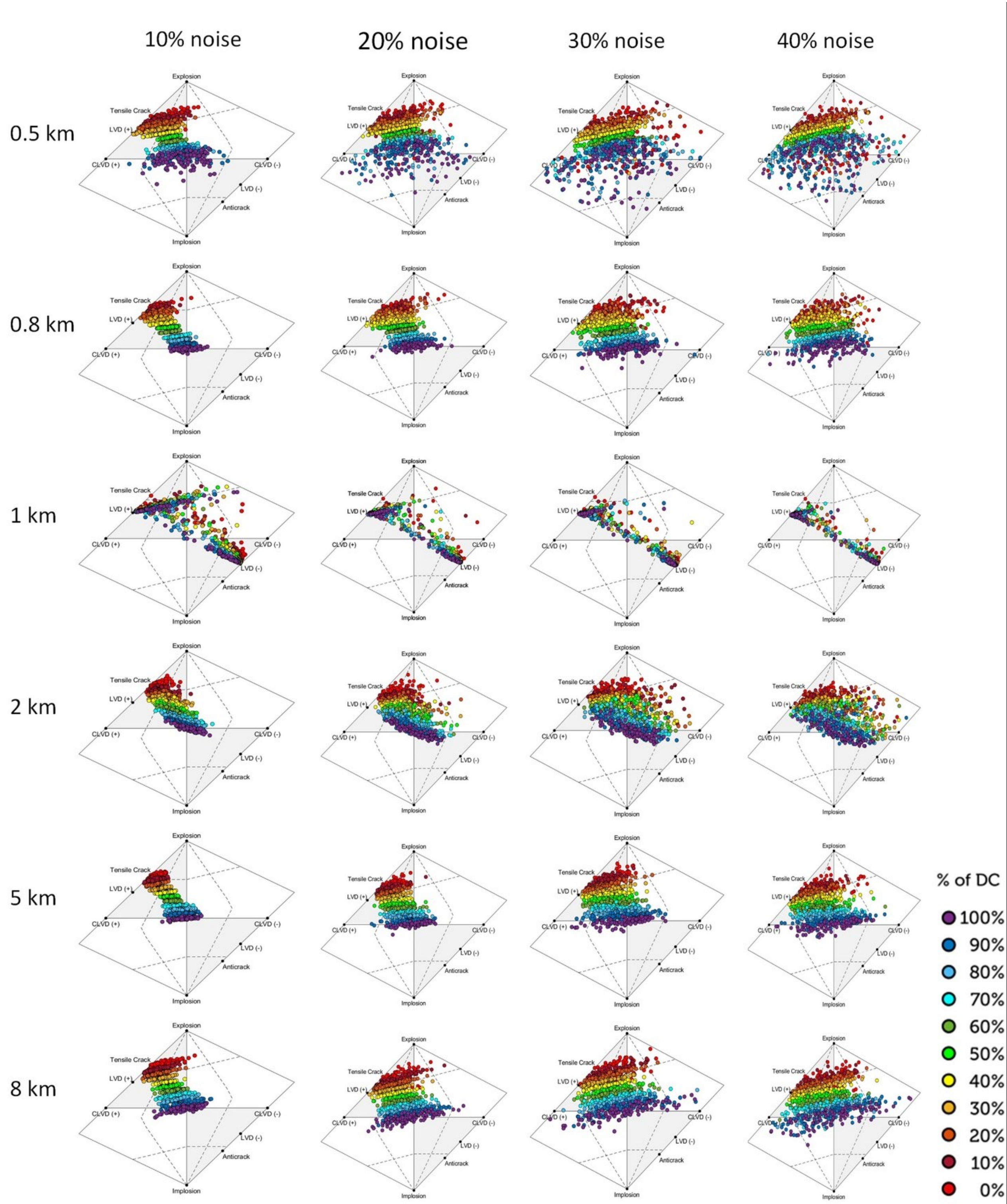

Figure 12 Synthetic tests diamond plots for LGCD, the normal fault for four noise levels and six depths.

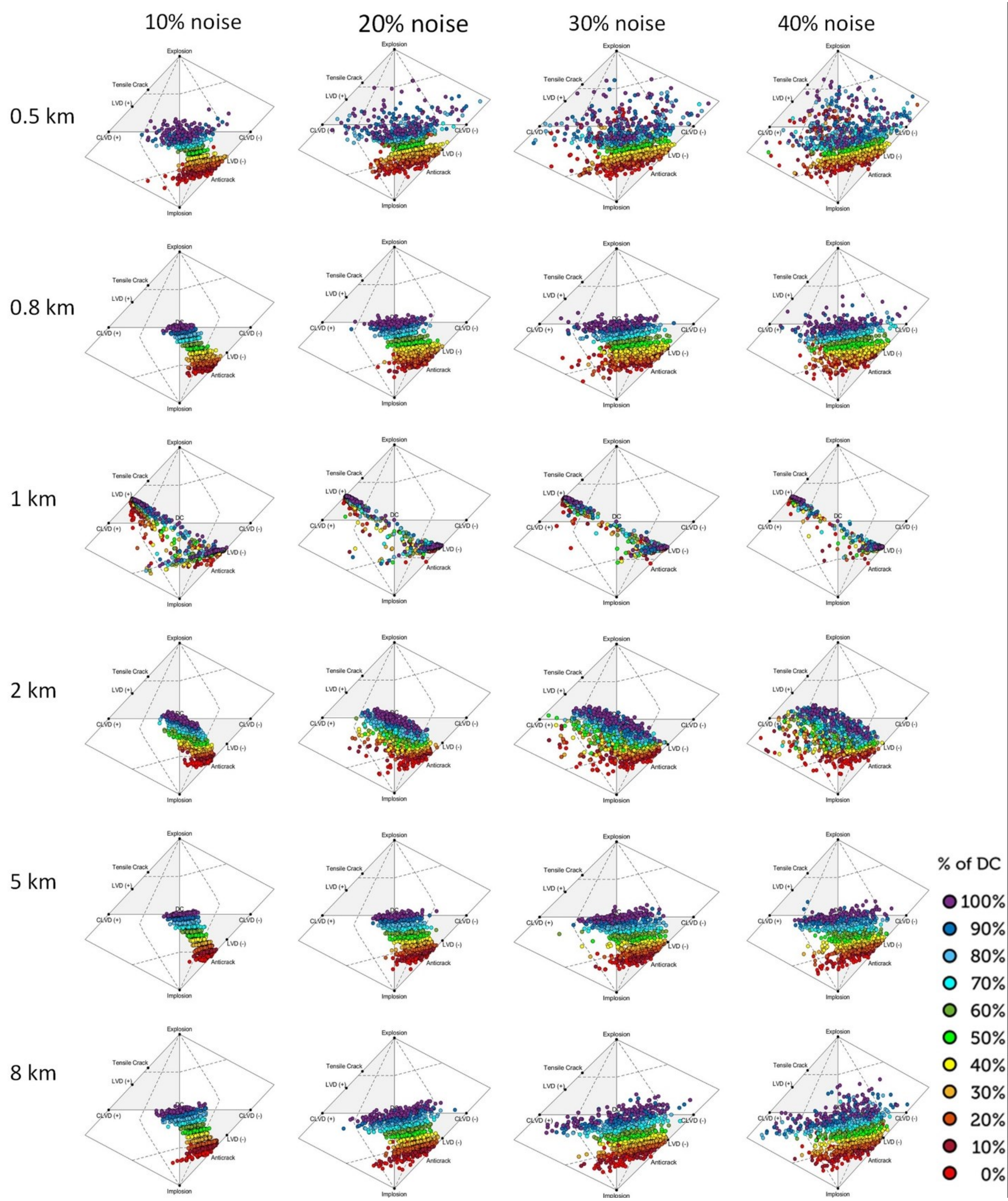

Figure 13 Synthetic tests diamond plot for LGCD, reverse fault.

3.1.2. Bogdanka Coal mine

The assumed geometry of fault for Bogdanka reflected the longwall face direction (60°/46°/±90°). Tests were conducted for two magnitudes: M_w=3.7 for comparison with other networks and M_w=2.9, representing the maximum recorded event at tests performing time. As minimal differences were observed in the results, further analysis focused on M_w=2.9. The event was placed within the currently active area, in the centre of the network. The focal coverage improved with depth, except for the 2 km, where the influence of the low velocity layer and the boundary is visible. Stability tests showed stable results for shallow events up to 1 km. For 2 km, where is the boundary of the low velocity layer, solutions are unstable even for 10 % of non-shearing components (Figure 11d). For deeper events instability occurs.

In the Bogdanka noise bootstrap analysis, both normal and reverse fault scenarios exhibited RMS errors below 0.2 for a 10% noise contamination level. With a 20% noise level, RMS remained below 0.3, while for 30% noise, it stayed below 0.4. At a noise level of 40%, RMS errors mostly remained below 0.5, with a few instances reaching 0.6. The RMS error values increased with higher levels of noise contamination. Events positioned on velocity layer boundaries showed improved RMS values for pure shear mechanisms.

The influence of the velocity model was evident in the obtained solutions (Figure 14, Figure 15). Again, no significant differences between normal and reverse fault types were noticed. Solutions at a depth of 500 m displayed two clusters regardless of the assumed mechanism and noise level (see Figure 14, Figure 15). For 0.8 km solutions tend to align with the LVD(-)-DC-LVD(+) line, further extended to the nonphysical part of the plot, creating a "V" shape. Substantial dissipation in calculated components was observed at a depth of 2 km, with numerous non-physical solutions. For synthetic tests with an assumed 2 km depth, solutions are arranged in almost horizontal lines with nearly half of unphysically solutions. Similar consistency in MT components with the assumed ones as observed at 2 km was noted for solutions at 1 km depth with some solutions aligned with the "V" shape observed for 0.8 km. The best solutions were obtained for a depth of 5 km, while at 8 km, solutions became more scattered again. Mechanisms comprising about 50% of double-couple component located at 5 km and 8 km seemed less sensitive to noise contamination. The "V" shape observed in the results is connected to the source-type plot facilities. The dashed near-horizontal line shows equal dilatation in the mechanism. Moreover outside the zone created by the upper and lower dashed lines P-wave radiation pattern cause all polarities positive or negative, depending on the region (Hudson et al., 1989).

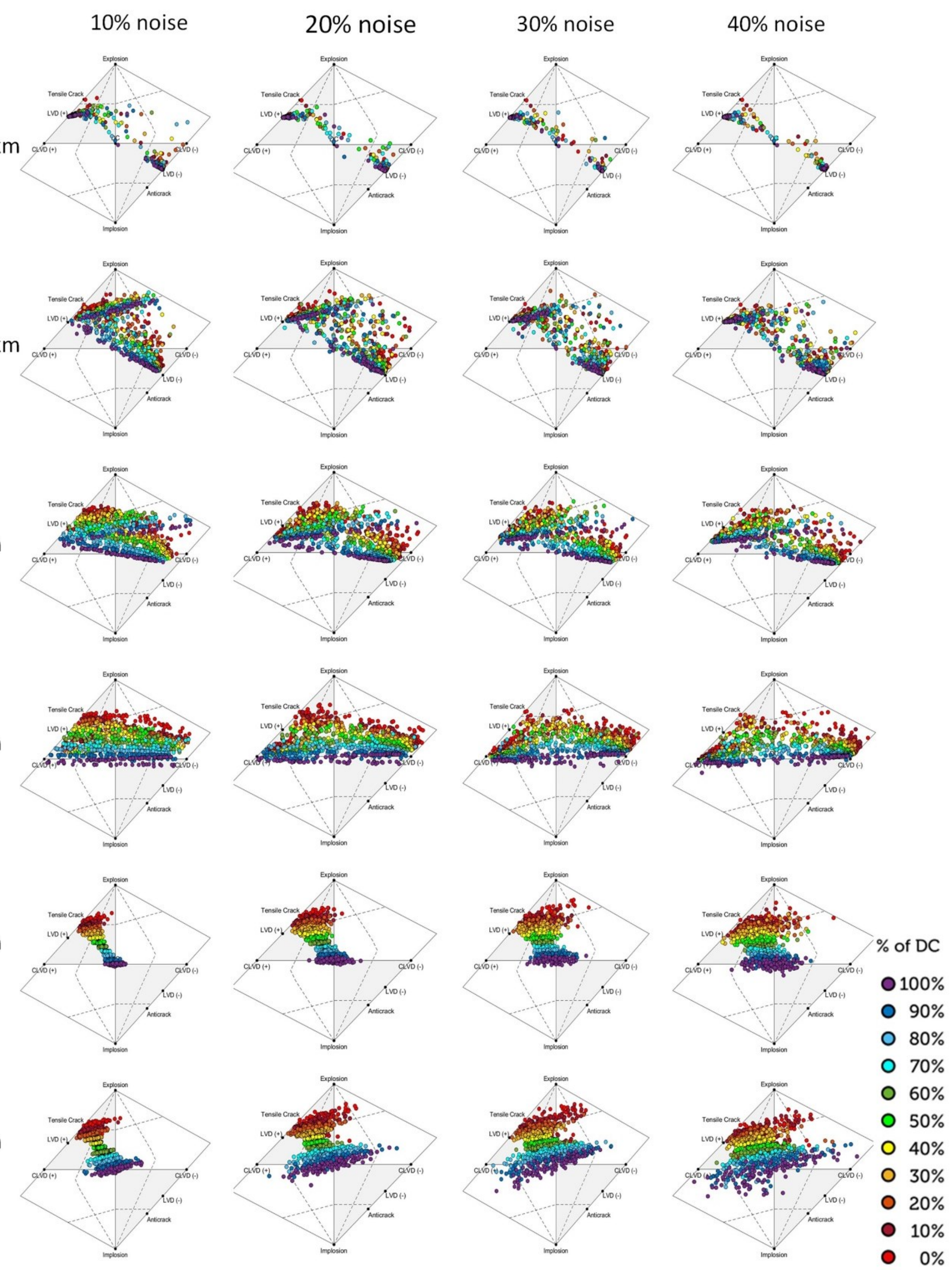

Figure 14 Synthetic tests diamond plots for Bogdanka, the normal fault for four noise levels and six depths.

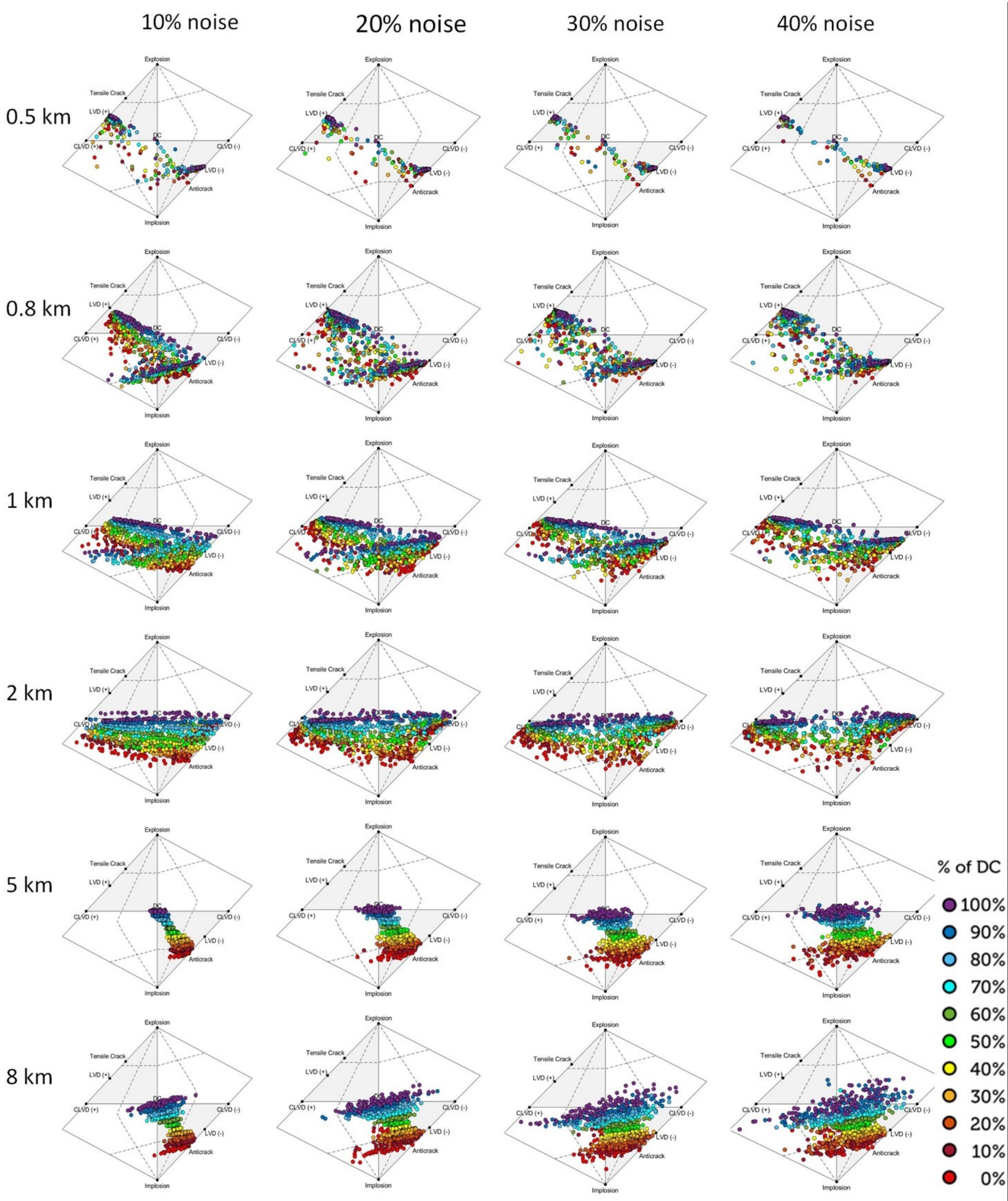

Figure 15 Synthetic tests diamond plots for Bogdanka, reverse fault for four noise levels and six depths.

3.1.3. Song Tranh 2 reservoir

A normal and reverse fault geometry with strike/dip/rake of 304°/71°/±108° was assumed for the test event, similar to most existing solutions (Lizurek et al., 2017). The event was located near the reservoir, in the centre of the network, and assigned a magnitude of M_W=3.7. Focal coverage changed gradually with depth as the homogenous velocity model was applied. The stability of events is better than for mine cases (Figure 11a). Shearing events with a DC component of more than 70% are resolved without perturbances. Rotation angle is below 20° for all cases shallower than 1 km. For deeper events rotation angle increases meaningly.

In the Song Tranh noise bootstrap analysis, a noise level of 10% resulted in an RMS value below 0.15 for both normal and reversed fault geometries. When the noise contamination increased to 20%, the RMS values remained below 0.3 for normal fault geometry, but some values reached up to 0.4 for reverse fault geometry. At a noise level of 30%, RMS values increased to 0.4 for both normal and reverse fault geometries. Generally, RMS values showed an upward trend with increasing noise level and event depth.

The agreement between the moment tensor decomposition results and the assumed values was most pronounced for event depths of 5 km, 8 km, 10 km, and 15 km within the VERIS network tests (Figure 16, Figure 17). However, as the noise level increased, differences in calculated components became more apparent. For event depths exceeding 2 km, these differences were minimal, while for shallower events, the range of MT solutions became more dispersed. Additionally, the dissipation of solutions increased with the involvement of non-DC components for shallow events. The shallower the event, the more visible an alignment of solutions with observed before the “V” shape. Notably, there was no visible difference in the stability or MT decomposition results between normal and reverse fault geometries.

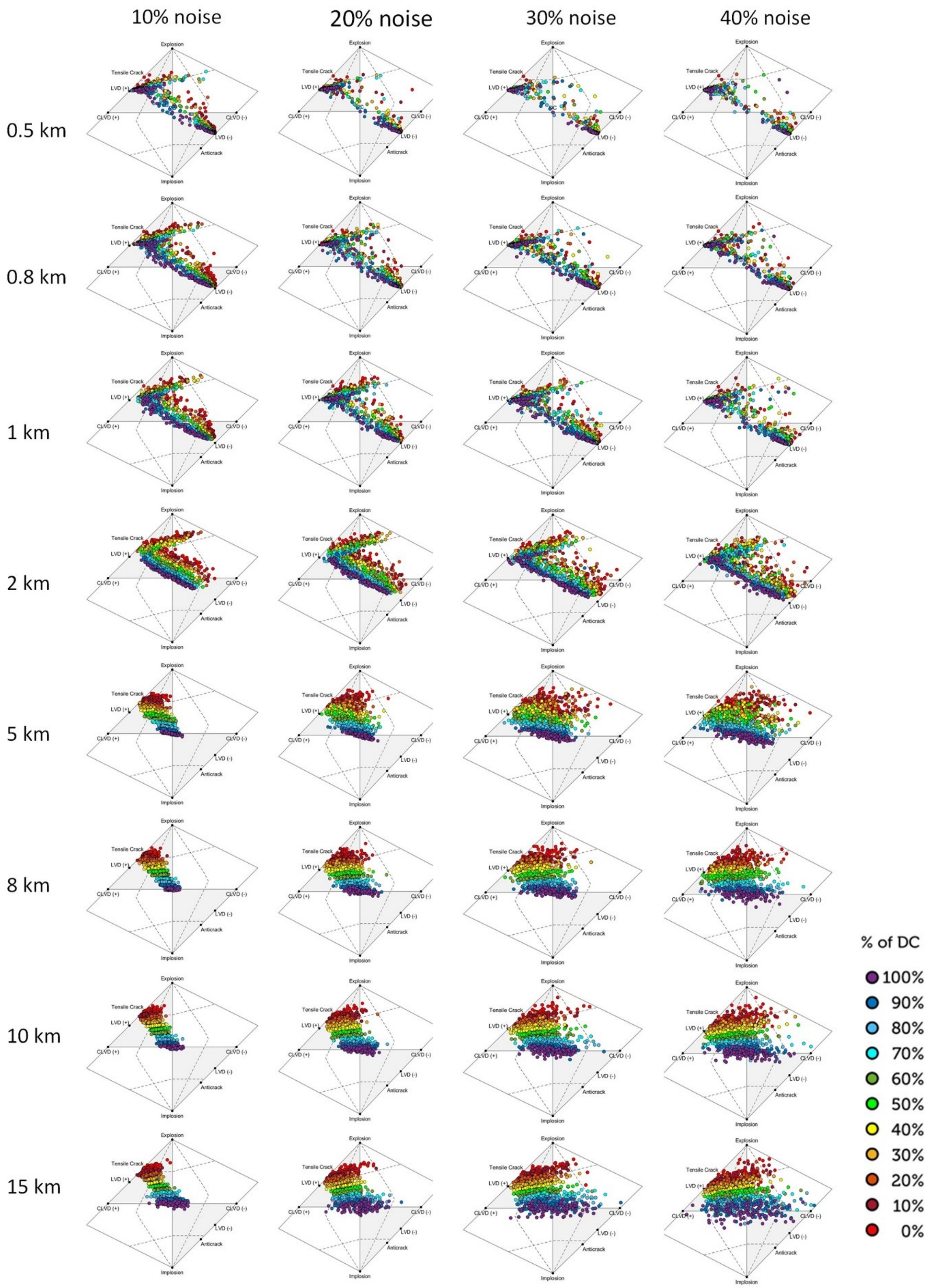

Figure 16 Synthetic tests diamond plots for Song Tranh, normal fault for four noise levels and eight depths.

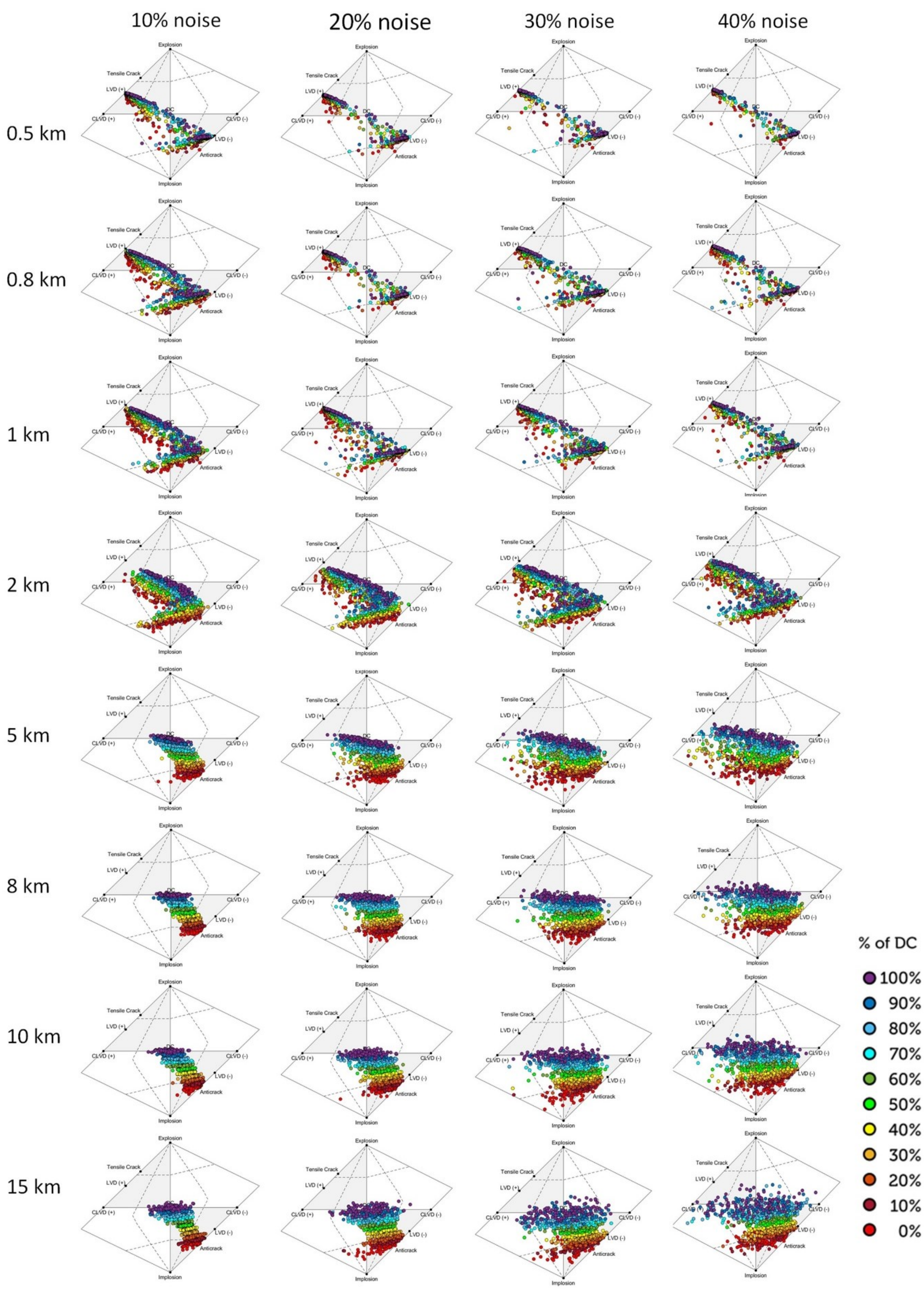

Figure 17 Synthetic tests diamond plots for Song Tranh, reverse fault for four noise levels and eight depths.

3.1.4. Lai Chau reservoir

The test event for Lai Chau also utilized a normal and reverse fault geometry with strike/dip/rake of 170°/46°/±90°. A magnitude of M_w=3.7 was assumed, and the event was positioned near the reservoir at the network's edge due to the absence of centrally located events with a determined focal mechanism. Strike-slip mechanisms were excluded to allow for comparison with other scenarios. The focal coverage changes smoothly with slight changes in the velocity model. Solutions are more stable than in the case of Song Tranh (Figure 11c). Almost all rotation angles are below 40° for mechanisms with a 30% DC component, besides the 15 km case where the layer boundary exists.

Similar to the observations for the Song Tranh network, noise bootstrap simulations in Lai Chau reveal a dependency of MT inversion stability on noise level and event depth. RMS error values remained consistent between normal and thrust fault geometries for a given noise level (e.g., 0.15 for 10% noise, below 0.3 for 20% noise, and mostly below 0.5 for 30% and 40% noise contamination). However, increasing depth generally led to a decrease in RMS error, particularly for source mechanisms with a non-DC component of approximately 50% compared to other mechanisms at the same depth and noise level.

Notably, a gradual improvement in the recovered MT components is observed with increasing depth, with a significant enhancement at a depth of 5 km (refer to Figure 18 and Figure 19). At shallower depths, the analysis yielded more scattered results. Two distinct clusters of solutions emerged for a depth of 500 meters and 40% noise. The dispersion of solutions was most pronounced up to 2 km depth. Interestingly, for a noise level of 10%, results tended to converge for shallow events. However, this characteristic alignment disappeared as the noise contamination increased, reorganizing into two clusters. Dispersion of solutions is more characteristic than for Song Tranh, which can be caused by the velocity model or earthquake location on the edge of the seismic network.

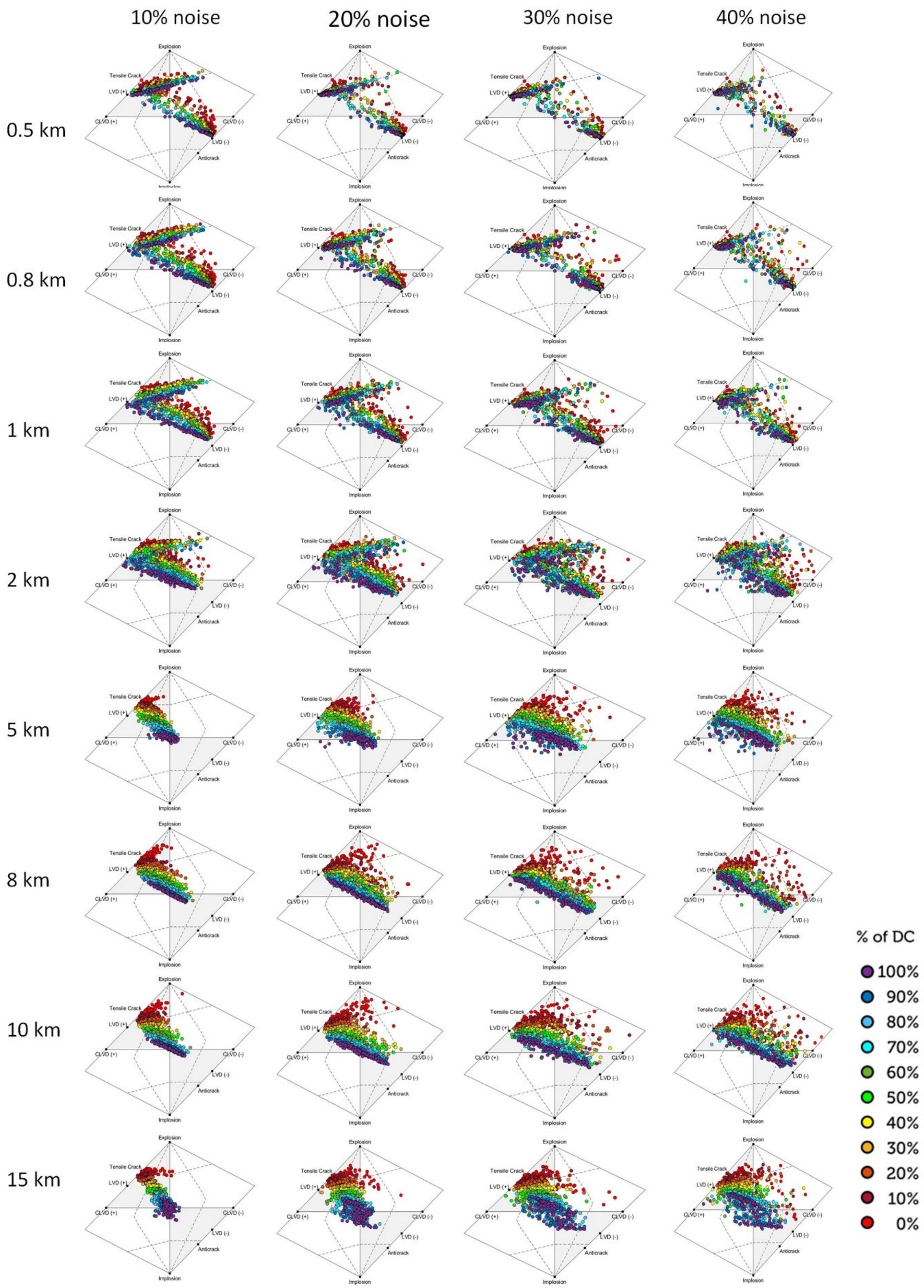

Figure 18 Synthetic tests diamond plots for Lai Chau, normal fault for four noise levels and eight depths.

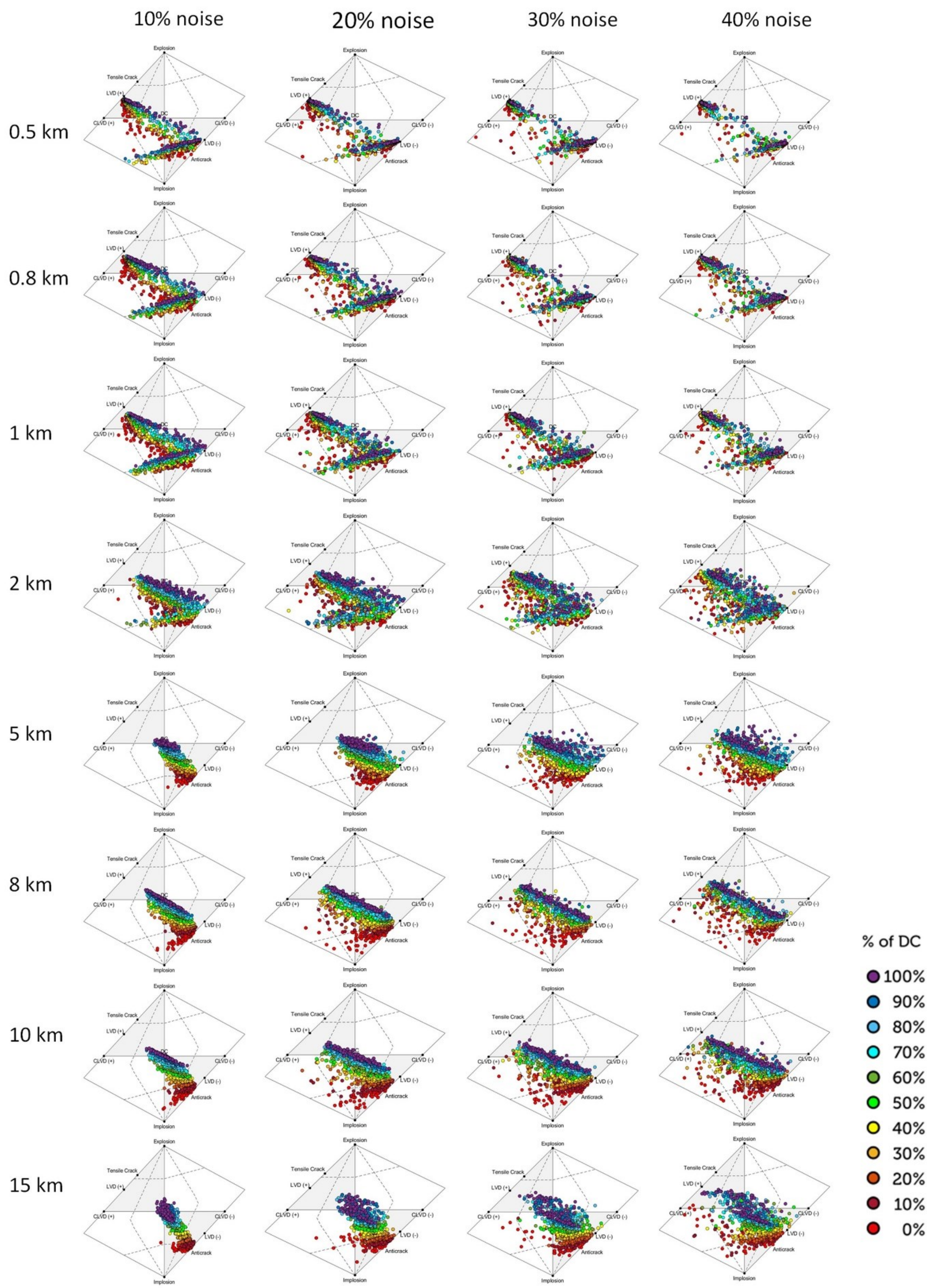

Figure 19 Synthetic tests diamond plots for Lai Chau, reverse fault for four noise levels and eight depths.

3.2. High-rate GNSS data in MT

Ensuring solution quality in moment tensor calculations relies heavily on azimuthal coverage. However, the number of stations available for MT inversion calculation can be significantly limited if the event occurs at the network boundary or if data from some stations is unavailable. Ground vibrations radiated from a seismic source can be recorded not only by seismological instruments. Remote sensing methods are used as complementary data in case of e.g. studying permanent deformations with InSAR methods (Ilieva et al., 2020) or Global Navigation Satelite Systems (GNSS) data used for fast magnitude estimation (Gao et al., 2021; Wei et al., 2022) and early warning systems (Li et al., 2019; Psimoulis et al., 2018). High-rate GNSS (HR-GNSS) allows for measuring short-period ground motion caused by earthquakes, however, such research was concentrated on strong natural events with amplitudes of approximately a few centimetres (Benedetti et al., 2014; Bock et al., 2011; Michel et al., 2017). The application of HR-GNSS to earthquakes with magnitudes of about 4 was confirmed by Saunders et al. (2016) and the possibility of recording small amplitudes of strong anthropogenic events recorded by the LUMINEOS network was confirmed by Kudłacik et al. (2021). In this research, two significant earthquakes recorded in the LGCD area were investigated using a combination of data from traditional seismic stations and HR-GNSS stations (Figure 20). The HR-GNSS data were prepared following the methodology described in Kudłacik et al. (2021).

For the first event, which occurred on January 29th, 2019, at 12:53:45 UTC, detailed analysis utilized spectral amplitudes from 17 seismic stations and 3 co-located HR-GNSS stations. This M_w 3.7 earthquake struck at a depth of 800 meters and resulted in a concerning mine corridor collapse extending 600 meters. Following initial Jackknife station rejection tests to ensure data quality, 12 seismic stations were chosen for the final analysis using only seismological data for MT inversion. This primary MT solution revealed a dominant CLVD component, which aligns with the subsequent roof collapse observed in the mine. Notably, key stations for this study included Komorniki (KOMR), Trzebcz (TRBC), and Tarnówek (TRN2), where strong-motion seismic stations were conveniently co-located with HR-GNSS stations. To understand the influence of missing data, the MT inversion under various scenarios was calculated where data from each co-located station was excluded or replaced with GNSS data. Detailed analysis for this event included full, deviatoric, and double-couple MT solutions with rotation angle calculations between reference mechanism calculated from seismic data and other combinations (Figure 21).

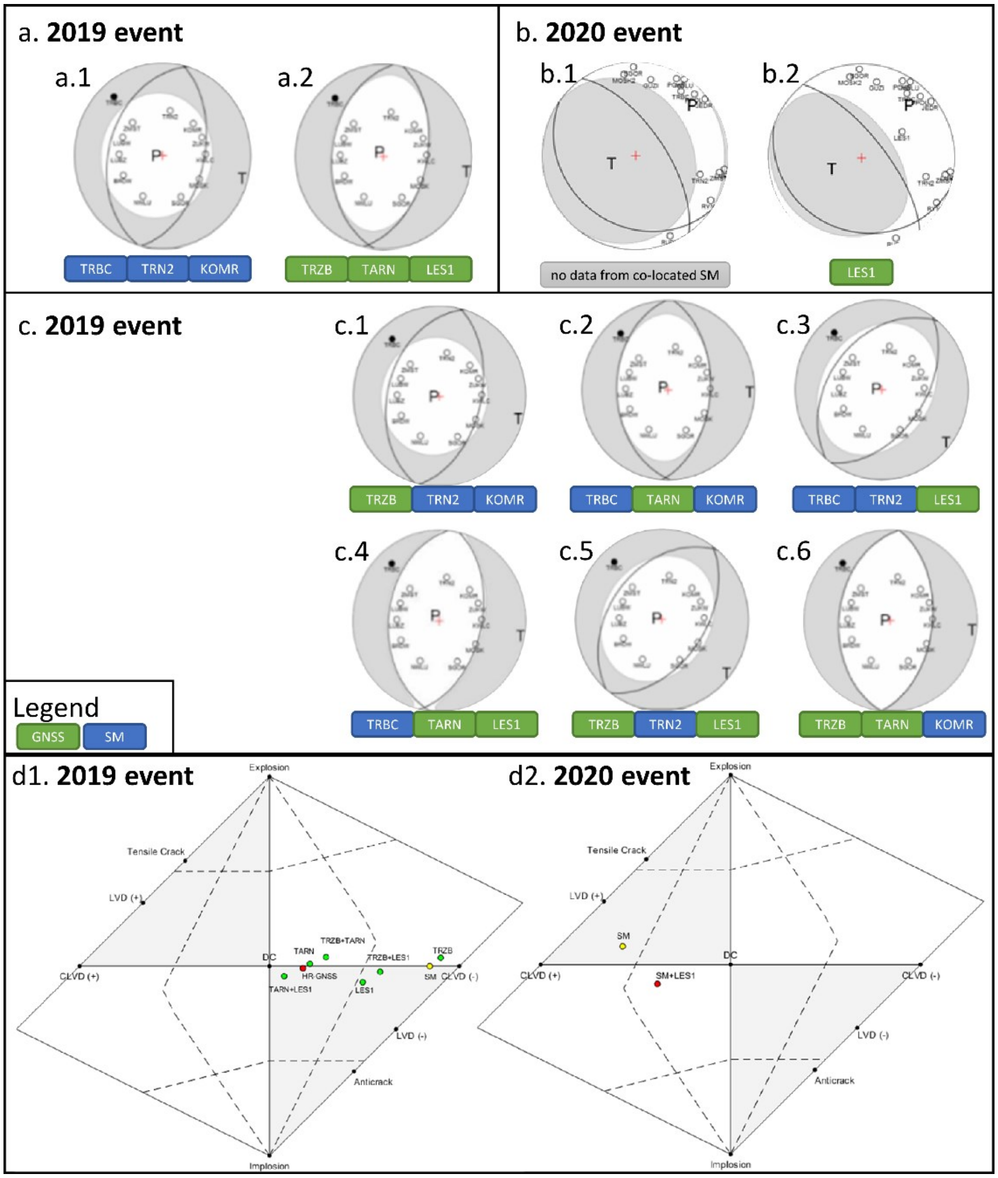

Figure 20 Full moment tensor solutions for 2019 and 2020 events a) pure SM solution and all GNSS applied data solution for 2019, b) SM solution and solution with additional GNSS station for 2020 event, c)solutions for different configurations of applied GNSS data in 20219 event, d)source-type plots for different solutions for 2019 and 2020 events.

The RMS values of the MT solutions are consistently low, indicating their stability and reliability across almost all cases. Specifically, the RMS reaches 0.17 for a solution utilizing 12 SM stations and 0.20 for a solution incorporating 9 SM stations and 3 GNSS stations. Mixed combinations, such as 11 SM stations with 1 GNSS station or 10 SM stations with 2 GNSS stations, exhibit RMS values ranging between 0.14 and 0.29. When HR-GNSS data replace seismic records in calculations, the MT solutions remain consistent with other results. The rotation angle between nodal plane solutions derived solely from seismic data and those incorporating HR-GNSS data remains below 23°. However, the Jackknife station rejection test reveals solution instability without the inclusion of the TRBC station, emphasizing the crucial role of this station in MT inversion, as closest to the epicentre.

The application of HR-GNSS data enhances solution stability, as evidenced by the case of 11 SM stations combined with the TRZB station (see panel c.1 in Figure 20). Here, MT decomposition closely aligns with solutions derived from seismic data, with low RMS error and negligible rotation angles, indicative of solution quality. Notably, the LES1/KOMR station's inclusion was not essential for this event, given its characteristics and station deployment (Figure 20, panel c.3). However, the substitution of HR-GNSS data from the TRN2 station in place of seismic data results in solutions skewed towards double-couple mechanisms, unsuitable for roof collapse scenarios (Figure 20, panel c.2). The instability of non-DC components in these solutions is evident, as depicted in the source type plot. This instability is not solely attributed to the use of three HR-GNSS stations but is rather a general feature of MT inversion in shallow events recorded by the LUMINEOS surface network, as demonstrated in the prior chapter. The sensitivity of non-DC components to both noise and focal coverage is consistent with performed synthetic tests.

The second earthquake was recorded on July 8th, 2020, at 05:18:59 UTC. This M_w 4.0 earthquake occurred at an unusual depth of 2255 meters, almost a kilometre below the active mining level. Unfortunately, the nearby and valuable seismic station KOMR was inactive during this event. The location of the event on the edge of the seismic network resulted in an unfavourable focal coverage for the earthquake. Despite this limitation, MT solutions were computed using spectral amplitudes from 13 seismic stations supplemented by the additional LES1 HR-GNSS station. Both solutions yield an identical RMS value of 0.28, which surpasses that of the previous event, potentially due to unfavourable focal coverage. Despite this, the mechanisms remain stable, with nodal plane orientations exhibiting similarity in both seismic-only and combined (SM+GNSS) moment tensor calculations, as evidenced by the low calculated rotation angle value (Figure 22).

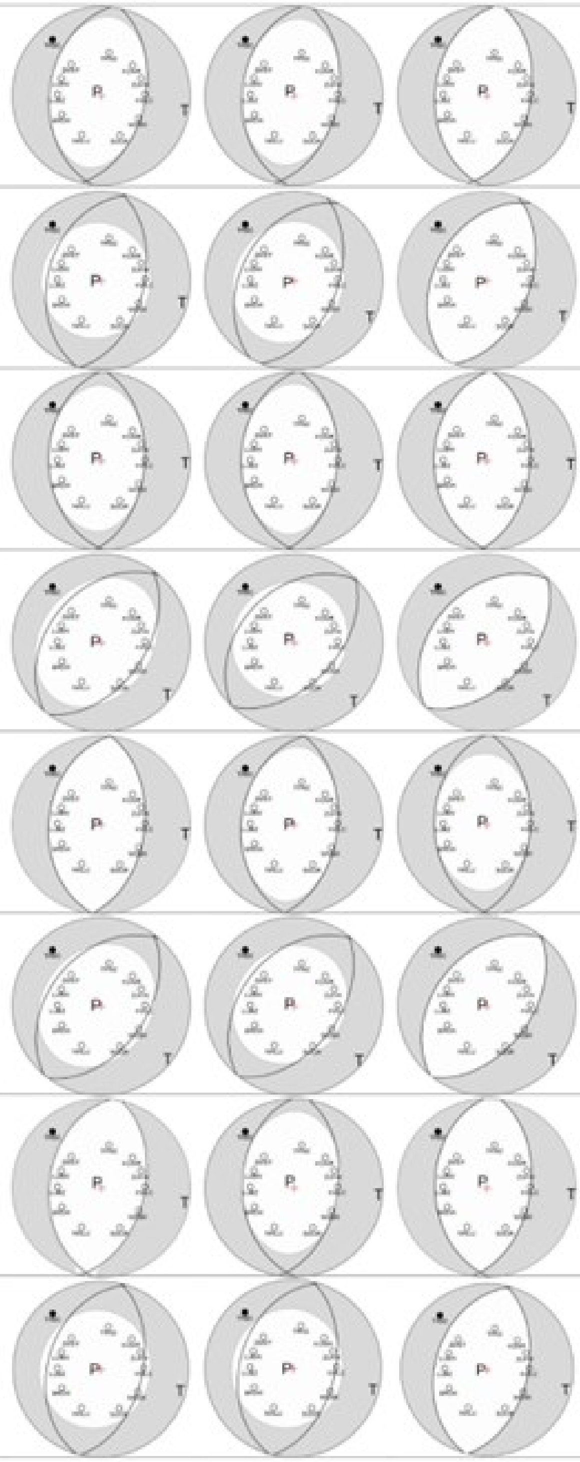

TRBC/ TRZB	TRN2/ TARN	KOMR/ LES1	Mw	MT components ISO/CLVD/DC	RMS	Full	Deviatoric	DC	Rotation angle
G	G	G	4.1	-1/-18/81	0.2				7.0
G	S	S	3.9	-4/-83/13	0.14				0.7
S	G	S	4.1	1/-21/78	0.29				13.88
S	S	G	4.0	-9/-49/42	0.16				22.94
G	G	S	4.1	4/-27/69	0.25				13.88
G	S	G	4.0	-3/-58/39	0.14				23.07
S	G	G	4.1	-5/-8/87	0.2				7.27
S	S	S	3.9	0/-84/16	0.17				-

Figure 21 Detailed MT solutions for the 2019 event with different sets of seismic and HR-GNSS data.

Notably, the mechanism derived from HR-GNSS data exhibits increased shearing compared to the solution obtained solely from the seismic network. Considering the placement of the LES1 station on the focal sphere, it's plausible to infer that additional information from the GNSS station enhances and stabilizes the MT solution. Full, deviatoric, and double-couple MT solutions for this earthquake are presented in two variations to showcase the impact of GNSS data.

The local magnitude calculations were overestimated. However, the overestimation of magnitude during MT inversion is a known phenomenon, especially in case of the weak, shallow events, here likely caused by complex velocity structures. Magnitude overestimation can be also related to the intermediate and near-field influence. Hence, magnitudes computed using varying sets of stations and velocity models may diverge. For instance, the magnitude reported for this event by EMSC was mb=4.9, whereas, in the local seismic catalogue featured in the EPISODES Platform (2017), it was listed as M_W=4.0. The incorporation of GNSS data demonstrably facilitated a more realistic overall magnitude estimation. Additionally, as seismic moment and moment magnitude are calculated based on the far-field assumptions, incorporating intermediate or near-field terms into the M0 calculation routine could prevent overestimating moment magnitude.

KOMR/ LES1	Mw	MT components ISO/CLVD/DC	RMS	Full	Deviatoric	DC	Rotation angle
G	4.8	13/48/39	0.28	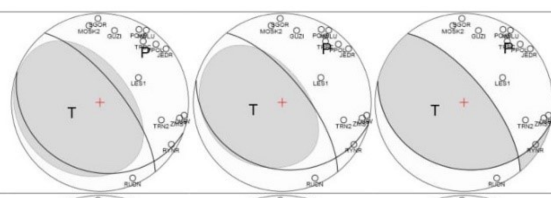			7.72
	5.2	28/66/6	0.28	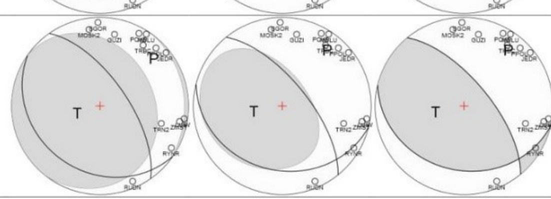			-

Figure 22 Detailed MT solutions for the 2020 event with two different sets of seismic and HR-GNSS data.

To determine the limitations of the application HR-GNSS data synthetic maximum amplitudes were calculated. Maximum displacement amplitudes usable in MT inversion for the discussed area were calculated for synthetic events with assumed mechanisms, depths, and magnitudes. Synthetic data were generated for magnitudes ranging from 2.5 to 4.5 and depths of

600 m, 800 m, 1 km, 1.2 km, 1.4 km, 1.6 km, 1.8 km, 2 km, and 2.2 km. The mechanism applied for synthetic event generation was a reverse fault (strike/dip/rake: 165°/50°/90°). The selected depth range covers the localization of tremors in the LGOM. Three different velocity models were applied. As expected, the highest amplitudes were observed for shallow events with high magnitudes. In an isotropic or gradually increasing velocity medium, the magnitude of vibrations on the Earth's surface decreases with increasing source depth, as shown in. However, in the LGCD area, seismic wave propagation in the high-velocity layer (depths of 800–1000 m) differs from this pattern. The elongation of the seismic wave path caused by the layer below the high-velocity layer results in stronger damping and lower amplitudes being registered on the surface. Figure 23 Maximum synthetic P-wave amplitude for different depths and magnitudes in the range 2.5 to 4.5 presented for three velocity models: real velocity model, isotropic, and gradient.illustrates that for a source located at depths of around 800–1000 m in the LGCD area, the P-wave amplitude on the Earth's surface will be smaller than it would be for a source depth of approximately 1200 m. The noise level was determined to be 1.5 mm, allowing only the shallowest tremors' first P-wave onset to be detected by the station directly above the hypocentre.

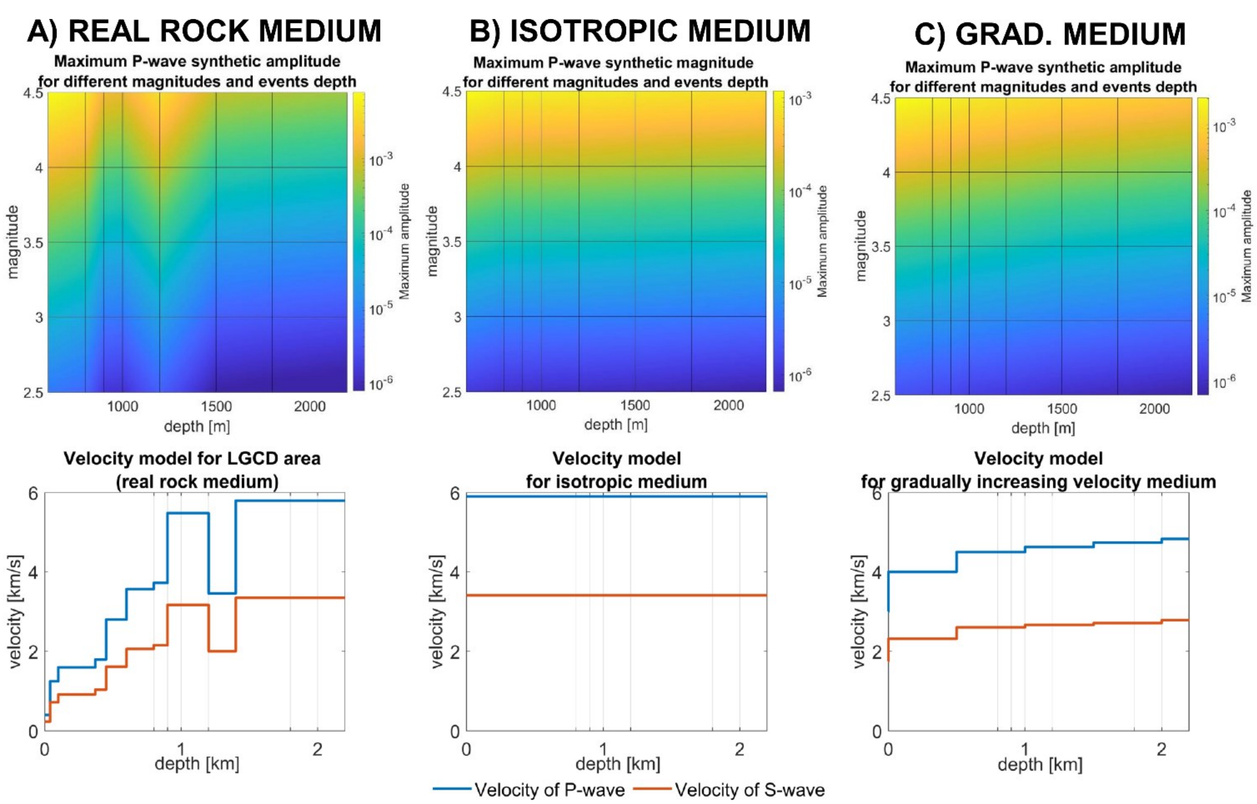

Figure 23 Maximum synthetic P-wave amplitude for different depths and magnitudes in the range 2.5 to 4.5 presented for three velocity models: real velocity model, isotropic, and gradient.

3.3. Intermediate field assumption

Another way to improve the moment tensor inversion is to include intermediate field assumption in a computation routine. For this part of the research, the Song Tranh and LGCD cases were selected. Song Tranh includes a plentiful database of calculated mechanisms that are necessary for the next steps. LGCD is the case where few mechanisms were calculated and data have been saved. The real case MT inversion was not performed on data from the Bogdanka mine and the Lai Chau catalogue contains only a few mechanisms. The first step was to determine the distance where the far-field and intermediate-field parts dominate in the recorded displacement amplitude. The below plots present the field ratio depending on the distance for the selected first-time peak duration (Figure 24). As most seismometers in the described networks have a sampling frequency of 100 Hz, the theoretical minimum rupture time possible to register is 0.02 s. However, taking into account the fact that the record of such a short rupture would consist of two samples, the actual minimum time of the fault rupture that can be recorded is longer. The maximum presented time is bigger than the biggest registered first peak duration and is enough to consider source dimensions up to 1 500 m for the LGCD area and 2 300m for the Song Tranh area.

The second part of intermediate field term influence research on amplitudes was to calculate theoretical amplitudes for far-field and intermediate fields. All assumptions introduced in the methodology chapter were applied. The first peak duration was taken from existing data- moment tensors calculated by first P-wave amplitude inversion. Location of events and stations, M_0, and velocities in sources were applied. Results were compared with measured amplitudes.

The LGCD synthetic amplitudes with intermediate field part were based on four events (Figure 25). The maximum intermediate amplitude was 63% of the total amplitude and the minimum was 7% (Figure 27). The intermediate field amplitude varies a lot depending on the station location. Most of the total amplitudes include at least 20-30% of the intermediate part. The theoretical amplitudes were all in the same range as the measured amplitudes. The amplitudes calculated for the July 2020 event seem bigger than the measured amplitudes, as this event was one of the strongest and located deeper than usual for this network. Additionally, the mechanism of this event is strongly non-shearing, meanwhile, theoretical amplitudes are calculated for the DC mechanism.

a)

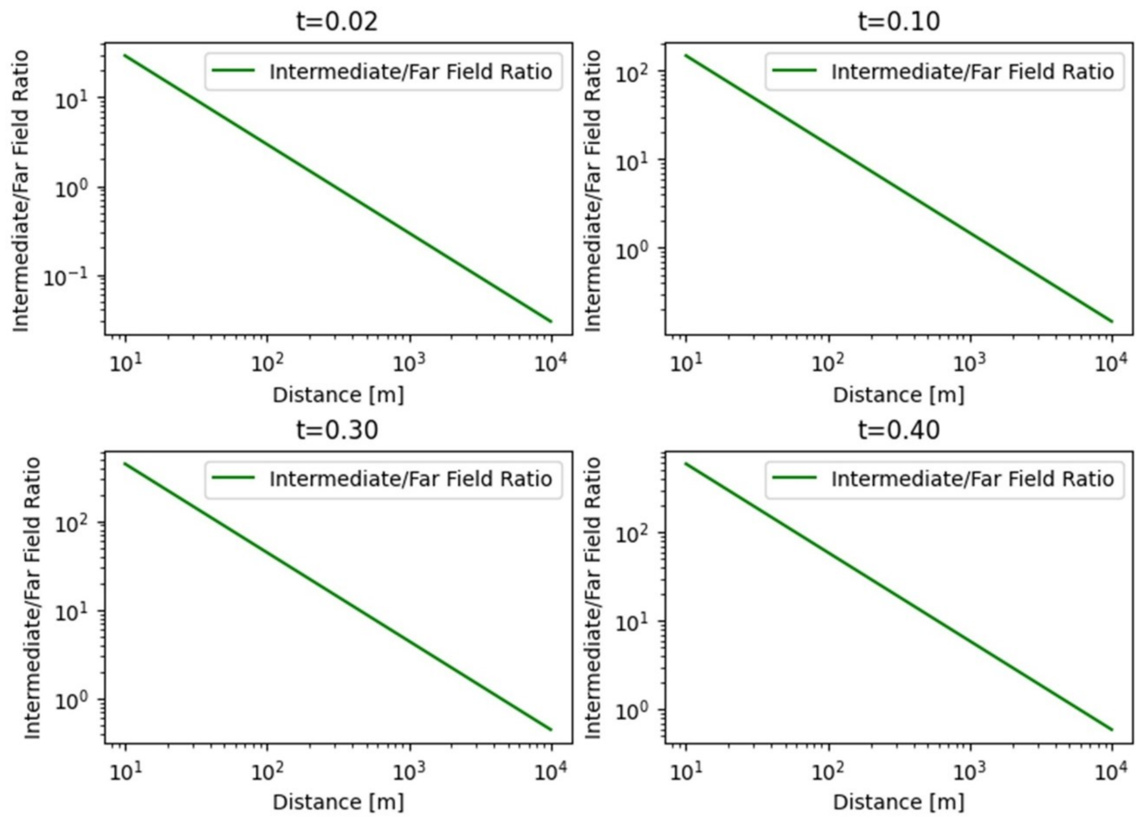

b)

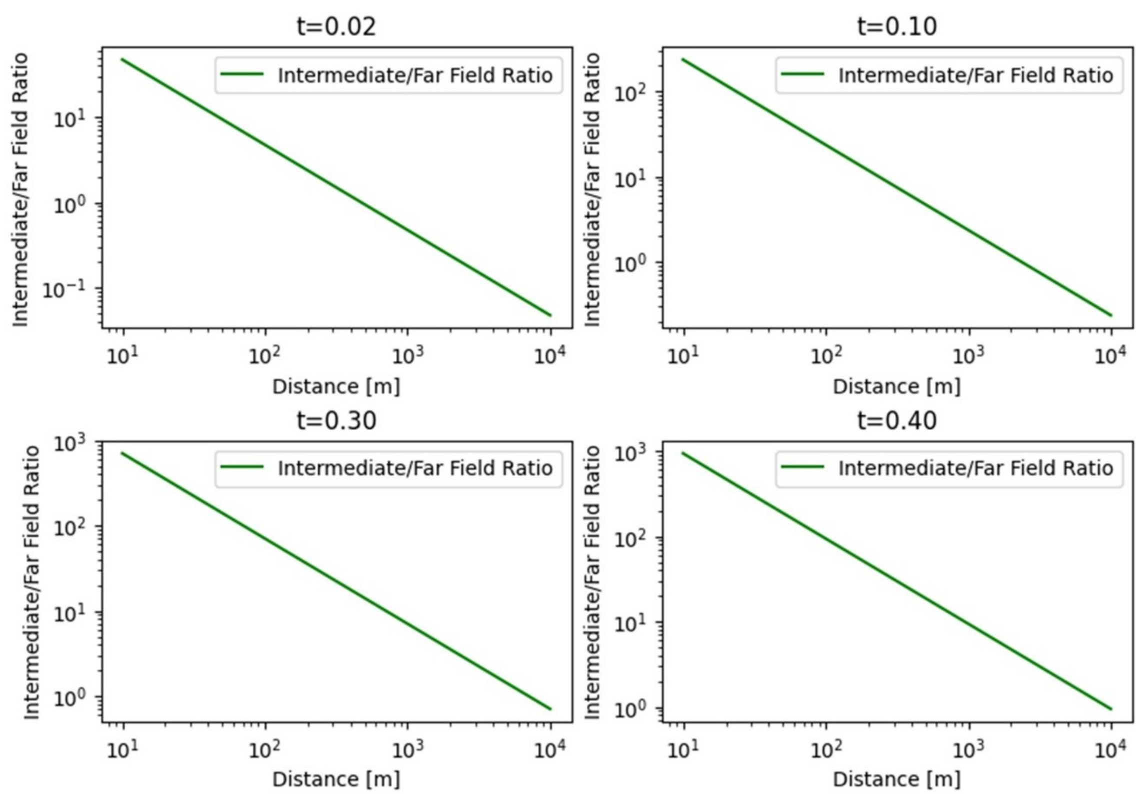

Figure 24 Far and intermediate fields influence depending on the source-station distance with radiation pattern coefficient equal 1 for far-field and 4 for intermediate field. Plots for a) LGCD, b) Song Tranh.

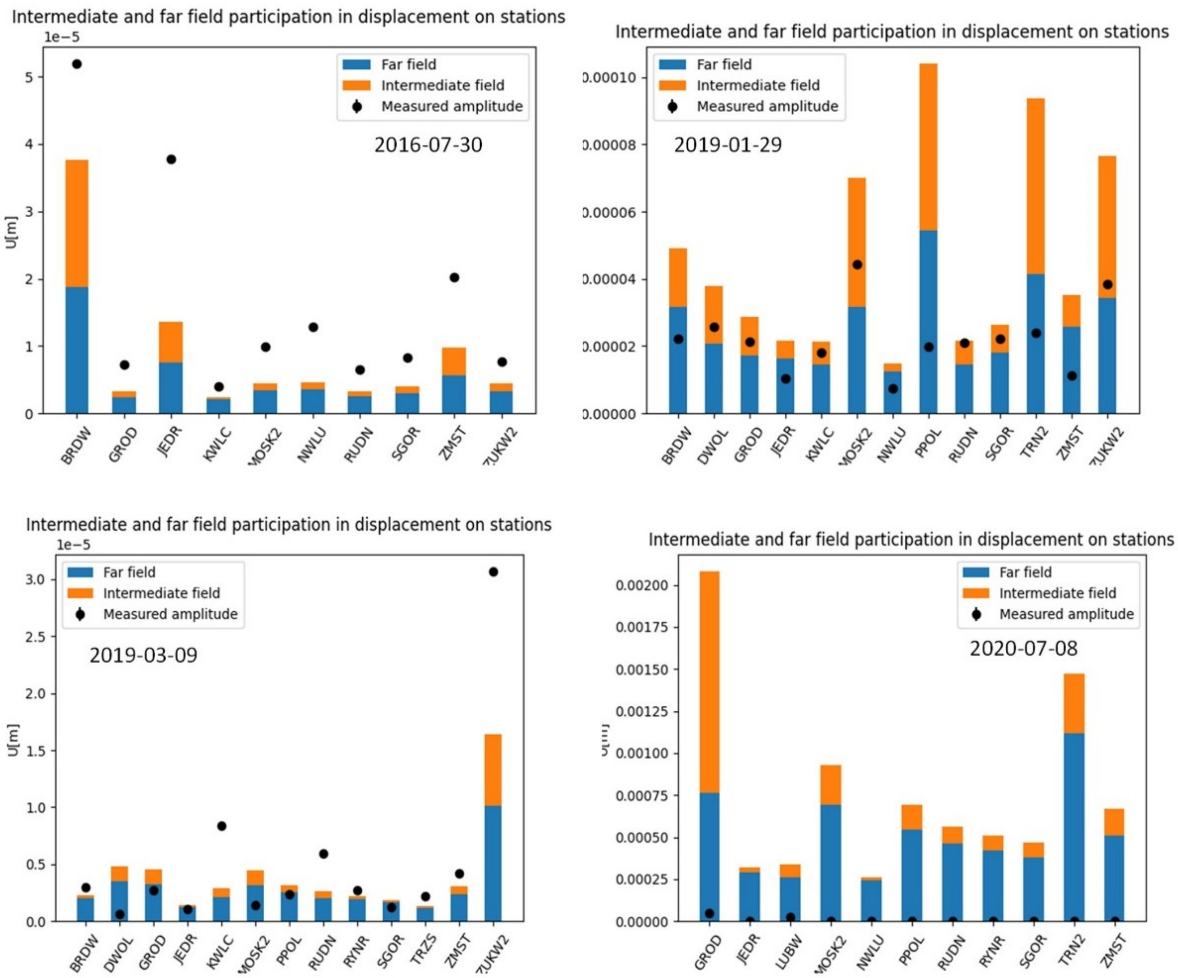

Figure 25 Amplitudes calculated based on far and intermediate field assumptions for four selected events from the LGCD area.

The Song Tranh results for intermediate field influence on amplitude value research was based on 180 events and selected results are presented in Figure 26. Most of the calculated amplitudes include less than 10% of the intermediate amplitude, and the maximum value of the intermediate field does not exceed 40% of the intermediate field amplitude (Figure 27). The theoretical amplitudes were all in the same range as the measured amplitudes.

Some of the apparent differences between calculated and measured amplitudes were observed in both the LGCD and Song Tranh dataset. Due to the limited number of events (only 4) in the LGCD dataset, its results were given less weight compared to those from the Song Tranh dataset. The differences between theoretical and measured amplitude were calculated and compared with event depth, moment magnitude and station-event distance.

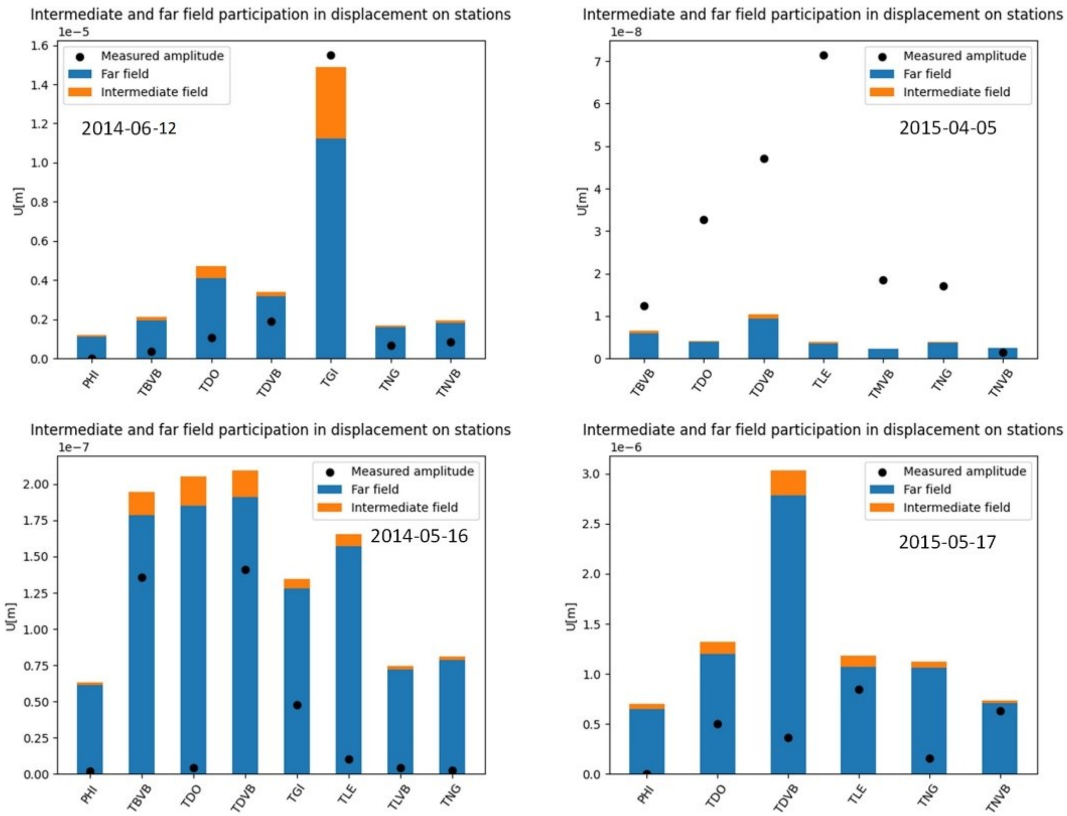

Figure 26 Amplitudes calculated based on far and intermediate field assumptions for four selected events from the Song Tranh area.

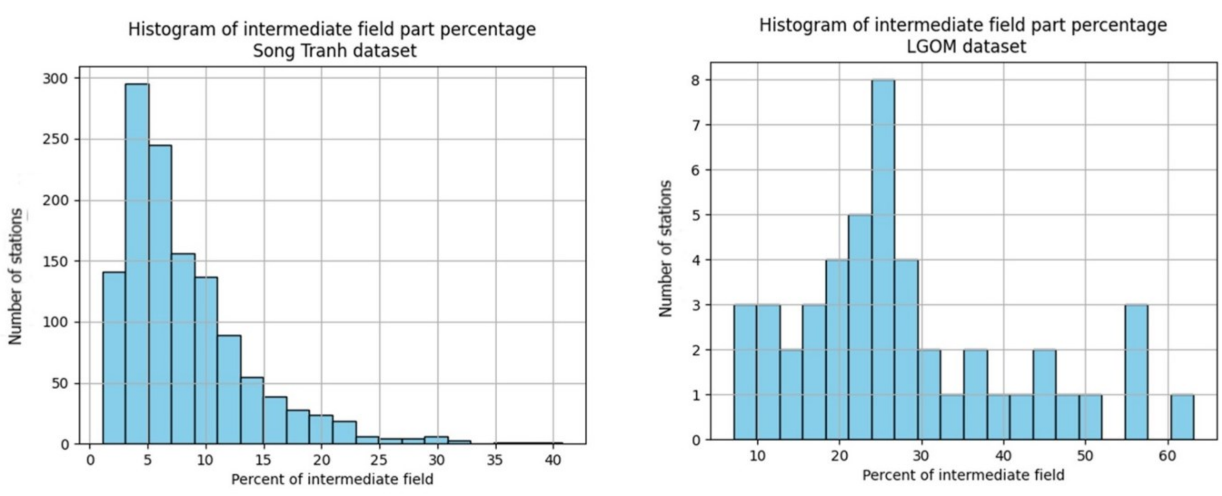

Figure 27 Histograms of the intermediate field amplitude part in total amplitude for two cases.

Event depth showed no influence on amplitude differences and its outliers (Figure 28 and Figure 29, top plots). On average, the difference in amplitude between calculated and observed values grew larger as the magnitude values of events increased (Figure 29, middle plots). The magnitudes calculated based on the scalar seismic moment and are overestimated, which is often observed case. However, event depth was important for a strong tremor in LGCD and reduced the intermediate field amplitudes. On the other hand, the applied radiation pattern coefficient made intermediate field amplitudes in the same range as the far-field amplitudes. For Song Tranh area intermediate field amplitudes were lower and had less impact on the total calculated values. The outliers with significant differences between calculated and observed amplitudes are more often in case of short event-station distance in both cases (Figure 28 and Figure 29, bottom plots).

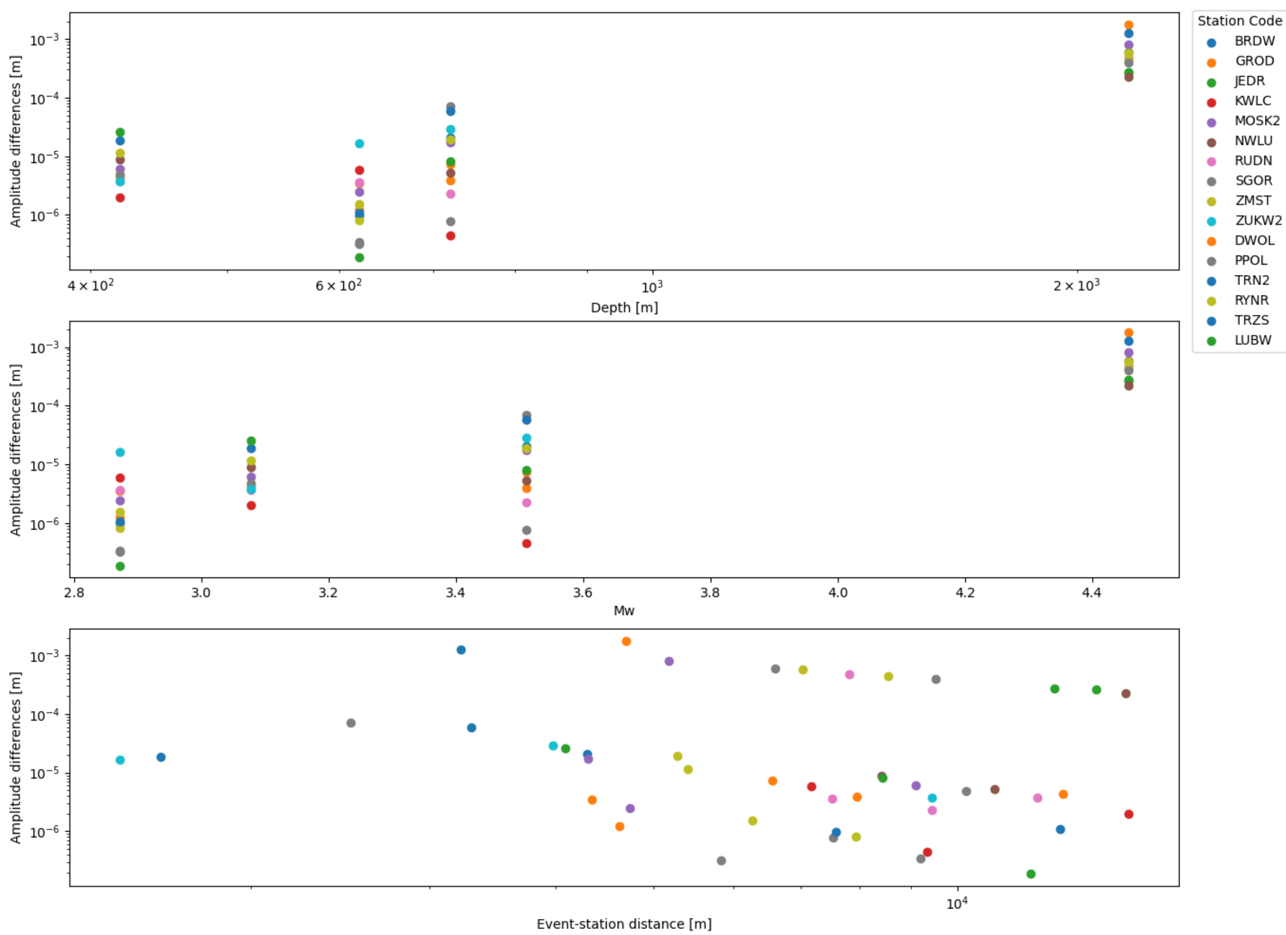

Figure 28 The LGCD calculated and measured amplitude differences compared with depth, moment magnitude and event-station distances.

Amplitudes calculated for the LGCD area were usually bigger than measured ones, especially amplitudes connected with event M=4. Such an effect could be caused by the unknown amplification and other site effects. In case of Song Tranh, some significant differences between calculated and measured amplitudes indicate higher values of the measured amplitudes. For Song Tranh differences plot with the moment magnitude shows that measured amplitudes increased faster than calculated ones (Figure 28 and Figure 29, middle plot). There were a few stations in Song Tranh where outliers were observed repeatedly: PHI, TBVB TDVB and TNG. Two of these stations were usually close to the event (TBVB and TDVB), meanwhile PHI was one of the distant stations. The LGCD dataset is too small to find any regularities in stations.

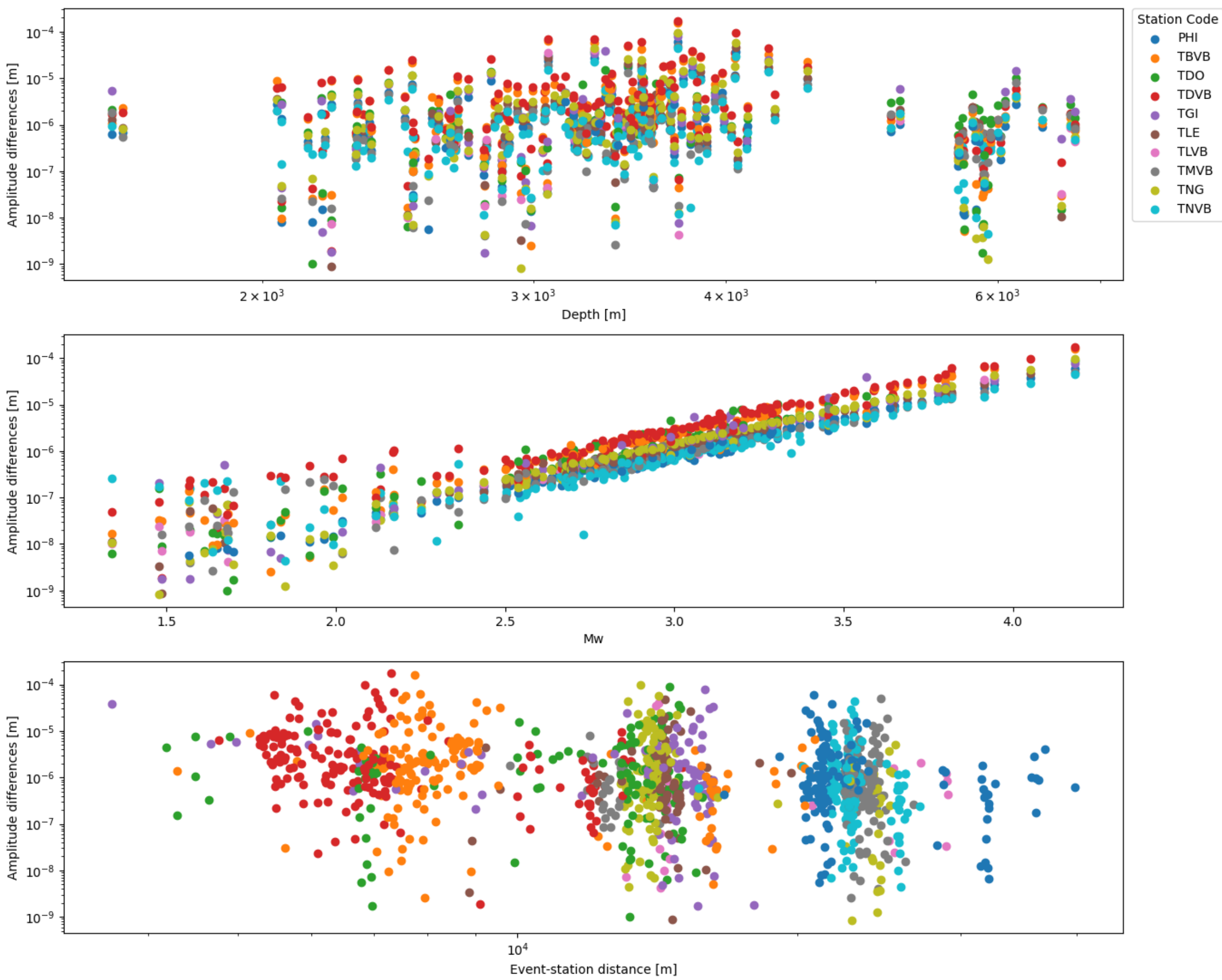

Figure 29 The Song Tranh calculated and measured amplitude differences compared with depth, moment magnitude and event-station distances.

4. Discussion

This discussion analyses the results presented in the preceding chapters concerning the non-double-couple components in seismic moment tensor inversion for anthropogenic seismicity. The reliability of MT inversion solutions was assessed across four networks with different geological conditions, identifying key factors influencing solution quality. Two methods to enhance the MT calculation methodology were proposed and analysed for potential application.

Solution quality determination is relevant for calculating MT for anthropogenic phenomena with substantial non-DC components. Synthetic tests on MT inversion indicated increasing instability with a rising contribution of non-double-couple mechanism components. Instability in solutions was observed especially if the depth of the event was greater than the biggest event-station distance for all networks, which is in accordance with another research (Ren et al., 2022). The gradually increasing velocity model allowed for more stable solutions for events deeper than 2 km contrary to the isotropic velocity model applied in Song Tranh. Despite unfavourable focal coverage in Lai Chau, caused by event location on the edge, stability for shallow events was preserved. For stable shallow events, stations on beach balls are arranged in a circle near the edge with big takeoff angles. For deeper events stations are spread uniformly over the sphere, with divergent polarities. For mine cases, instability was observed for 2 km in the Bogdanka case and for 500m and 800 m in the case of LGCD. These depths resulted in different focal coverage patterns. Stations are arranged in a circle with a lower takeoff angle, near the middle of the beach ball. The expected rule for the stability was the presence of stations with various polarities, however, results obtained during stability analysis deny such an interpretation. Significant for stability seems to be stations on the focal sphere evenly distributed in a circle near the edge.

The stability of MT inversion results is easy to notice. During the interpretation of calculated components, we do not have such possibility without additional information. For all four networks, the best component accordance with the assumed mechanism was observed for stations distributed over the whole sphere with at least one station with opposed polarity. However, cases with only one reverse polarity were observed as necessary for the LGCD network, it could be caused by other characteristics of the velocity model. Therefore generally more stations with contrary polarities should be required. As the synthetic tests show, the correctness of resolved components also depends on the focal coverage.

Focal coverage depends on the depth and the velocity model. In the homogeneous media of Song Tranh, a smooth change in focal coverage with depth is evident. In the simple model of Lai Chau, focal coverage changes gradually with velocity variations however, the azimuthal gap is visible. In Bogdanka, focal coverage improves progressively, except at a depth of 2 km, where the low-velocity layer and significant changes in take-off angles cause a shift in station locations on the sphere. Shallow event ray paths have almost horizontal take off angles and large (vertical) incidence angles. The exception is the Rudna mine, where changes in focal coverage for events reflect the complexity of its velocity model. The near surface velocity model for LGCD is detailed. Additionally, the presence of a low velocity anhydrite layer just under a high velocity layer strongly influences seismic wave path, which results in small incidence angles for sources located at depths 500 m and 800 m.

Next to RMS error, stability and component reliability should be considered when the quality of MT inversion is assessed. Components were resolved well if the uniform distribution of stations over the focal sphere existed. To get a stable solution the reverse arrangement of stations on the focal sphere was required, which apparently excludes obtaining a stable solution with certain components. As the stability is easily noticeable contrary to the components, the condition to require high incidence angles have confidence about stability is not necessary.

For analysed networks, two established for artificial reservoir monitoring show sufficient conditions for the analysis of deep tremors with a dominant shear component. Such events are observed in areas of Lai Chau and Song Tranh. On the other hand, complex velocity models in mines make shallow events unreliable, especially if high seismic noise is present. Compared to the test results from the Rudna mine, it is essential to examine the influence of a detailed near-surface velocity model to determine if its inclusion can enhance the quality of MT solutions. These areas may experience increased seismic noise due to ongoing exploitation activities, making it crucial to reinforce MT solution quality. Any additional data to upgrade focal coverage should be examined.

Synthetic tests covered four local networks: two mining and two reservoir monitoring networks. The studies did not include network geometry analysis and assumed a single event location coinciding with observed tremors, except for analysing event depth influence, closely linked with the adapted velocity model and influencing the focal coverage. This allowed to identify focal coverage patterns advantages. The synthetic test methodology assumed a specific mechanism, allowing precise solution quality determination but restricting the set of mechanisms.

The P-wave amplitude inversion method limits the use of data with low signal-to-noise ratios and events at depths not exceeding the maximum event-station distance. Understanding the influence of applied velocity models on focal coverage is critical, as high velocity gradients can lead to inaccurate component determination despite seemingly correct solutions. Due to significant variability between local seismic networks, the accuracy of seismic moment tensor solutions should be individually analysed for each network.

In MT calculation, especially for shallow events azimuthal coverage is crucial for solution quality. Unfortunately, the event's location at the network boundary or data unavailability from some stations can significantly limit the number of stations available for MT inversion calculation. As one of the proposals, the use of high-frequency GNSS was considered to support mechanism calculations. Two strong events with magnitudes M_w=3.7 and M_w=4 were recorded by GNSS stations in the LGCD area and could be used in the research. Because of the characteristics of the HR-GNNS time series, a small first P-wave amplitude could be missed. To avoid mistakes the first onset amplitude was replaced with the spectral level Ω value (Gibowicz & Kijko, 1994). The general geometry of the focal mechanism is well resolved in all cases when compared to the MT inversion solution obtained with regional broadband stations published by Ilieva et al. (2020). The full, deviatoric, and double-couple solutions are similar, which shows that GNSS data may be added for MT inversion in place of seismometers if needed without significant loss of the solution quality. However, it is valid only in cases of events of magnitudes over 3.5 and when GNSS stations are close enough to seismic sources in the mining areas, as synthetic maximum amplitude analysis revealed. One of the calculated mechanisms revealed one station crucial for event stability. In such cases, additional information is vital to get the mechanism of the event.

One potential problem can be the choice of polarity for the spectral level to apply in MT inversion. Polarity depends on the radiation pattern and indicates areas of tension and compression. However, many methods have been proposed to determine the polarity correctness, including Bayesian methods which do not require signals (Pugh et al., 2016). In the case of applying singular HR-GNSS stations in the MT inversion polarity could be easily determined.

Other limitations is the ability to identify the event in GNSS time series, as GNSS accuracy is smaller than seismometers, especially the vertical component. The determined level of noise was 1,5 mm for HR-GNSS measurements (Kudłacik et al., 2023). For the LGCD area, this limits the application of HR-GNSS to strong and shallow events. Geological features there make amplitudes generated by events at some depths smaller and harder to detect. However, for isotropic and gradually increasing depth medium main condition of amplitude detection is depth. In general, it suggests that if we would like to monitor the dynamic surface effects and focal mechanisms of high energy mining seismic events, GNSS stations located near the source area may be significant additional information useful for better quality of MT inversion.

Another approach to improve the MT solution quality may involve considering the intermediate field's influence. In most cases, the near and intermediate field terms are assumed to be insignificant and are ignored. On the other hand, near-field effects were observed on the distant station of big, deep earthquakes (Vidale et.al. 1995). The intermediate field influence may be significant for seismic networks registering shallow tremors at short distances, such as LGCD, although it should also be considered for larger networks. The share of the intermediate field amplitude in the total calculated amplitude in analysed cases reached up to 60%.

The distance at which we can assume simple far-field radiation is often described as the distance of a few wavelengths from the source. On the other hand, near-field is often connected with permanent static displacement and decays fast with the distance. However intermediate term carry both near and far-field influence and there are no “intermediate” distances. To determine the distances with the intermediate field term influence, the Haskell rectangular finite fault model was assumed, and based on the boxcar source time function some simplifications were made. The distances of equal far and intermediate field influence registered amplitudes depend on the P-wave velocity in a seismic source and a rupture time, so first peak duration. In real cases, for the Song Tranh area, distances up to 10 km could be influenced more by intermediate field term than far-field if the peak duration is about 0.4 s. For mine LGCD area, with lower velocities, equal influence from far and intermediate fields can be observed up to 7 km from the source. Even if we assume that the first registered peak duration is lower and events depths are significant, still some of stations will be placed in areas with intermediate field term strongly influenced the wavefield.

The analysis of the intermediate field was based on the shear mechanism, which is a commonly used model in seismology. This approach enabled the development of relationships for a simple source, allowing a focused examination of the effects of implementing intermediate field terms. Additionally, the shear mechanism is the most frequently observed type of tremor in the Song Tranh area, where the majority of data for analysis is available.

The theoretical assumptions were applied to recalculate amplitudes for real events based on the manually chosen peak durations and far and intermediate field equations. Some high participation of intermediate field amplitude was observed in both Song Tranh and LGCD areas. All calculated amplitude values were in the same order as the measured ones. Observed intermediate field term was generally smaller in Song Tranh and was about 5-10% for most of the cases. As the Song Tranh network covers a bigger area and events occur deeper values of intermediate field amplitudes were expected to be lower than in the LGCD case, where usually 20-30 % of amplitude comes from intermediate field term. In both cases, some of the amplitudes were calculated with substantial intermediate part. To assess the correctness of the calculated amplitudes differences between calculated and measured amplitudes were calculated. Some outliers are present, especially in the case of short event-station distance. One of the observations is the influence of the scalar moment tensor, or moment magnitude. This trend observed in the Song Tranh amplitude differences could be due to the initial method of calculating the seismic moment, which is based on far-field assumptions for stations, regardless of their distance from the tremor.

Differences between calculated and measured amplitudes can have various causes. The analysis of damping and amplification, which were undetermined in this research, could address some big differences in measured and calculated amplitudes. Amplification factors may not have a significant impact on the Song Tranh stations located on old crystalline bedrock. However, in the LGCD area, the surface layer of Quaternary sediments can significantly affect the recorded amplitude values.

Except for the site effects also assumptions can carry some uncertainties. Since the ratio between intermediate and far-field influence on amplitudes depends on the source velocities and time peak duration, accurate velocity determination is crucial. The source velocity for analysed cases is based only on a 1D velocity model. For instance, the Song Tranh velocity model is not connected with borehole measurements, and the LGCD velocity model was prepared for the northern part of the area. Errors in time peak duration may also arise from data processing. Additionally, the event-station distance is crucial for field calculations. While station locations are assumed to be undisturbed, the event location can include errors depending on the number of available stations and methods of location. Depth, in particular, carries significant uncertainty. Also, radiation pattern influence could cause some amplitude differences. Here, a simple coefficient was applied, however radiation pattern is not uniform in space. The value of the registered amplitude depends on the station placement concerning the source and fault orientation. Additionally, as Madariaga (1978) indicated, the Haskell fault itself causes two types of radiation. The weak spherical waves are radiated from the corners of the rectangular fault in the near-field, but the far-field registers only cylindrical waves in front of the fault. Even in the case of a simple source model, the near-field can add some unexpected fluctuations in theoretical amplitude values.

A point source assumes a very short rupture duration, which is crucial when calculating MT from the first P-wave arrival. Since the observer is far from the source, the details of the rupture process are encompassed by the source time function $M_0(t)$. A possible solution is to change the source time function or to model a finite fault using multiple point sources. In the case of an extended source, theoretical amplitude calculations in the inversion process, assuming a point source, can be significantly erroneous. The type of source directly influences the duration and amplitude of the first peak, and the equations used in the inversion will determine the specific tremor parameters. The Haskell model with a boxcar source time function can be used to model a more complex extended source and address the issue of excessively long first peaks of the recorded wave.

Attempts to incorporate the intermediate field into MT inversion require analyses for mechanisms other than double-couple. However, considering the intermediate field's percentage contribution to the presented calculations, its influence may significantly affect seismic moment tensor solutions.

5. Conclusions

The research focused on the non-double-couple (non-DC) components of the full moment tensor solution as artifacts of P amplitude inversion, aiming to determine the methodology's limitations and analyse possibilities to improve MT inversion methods.

The synthetic tests revealed several critical findings. Non-physical solutions occurred more frequently with high non-DC components in generated events. The velocity model significantly impacted solution stability, with mine networks showing worse stability due to the complexity of their velocity models. Solutions were unstable when events were located on velocity layer boundaries. A low-velocity layer, common for both mine scenarios, caused instability for events located within or below this layer. Moreover, instability was particularly noted when the event depth exceeded the maximum event-station distance. Low RMS error does not implicate solution correctness, as calculated components can describe physically impossible mechanisms. Thus, examining the impact of these factors is crucial for potentially enhancing MT solution quality.

The Lai Chau and Song Tranh networks set up for monitoring artificial reservoirs, provide stable and reliable MT inversion for the depth range of the occurring events. The main limitations of MT inversion for these networks are associated with shallow, non-DC-type events, which are unlikely in reservoir-induced seismicity along existing tectonic faults. While the location of an event on the network edge may affect the component results, it does not compromise the overall stability of the solution. Shallow events were resolved with incorrect components with a tendency to align in a V-shape on source-type plots or to create two clusters in case of high noise contamination.

The Rudna network effectively resolved components at a depth of 0.8 km, including exploitation levels. Shallower events at 0.5 km showed significant dispersion even in the case of low noise implementation, and the 1 km level is visibly influenced by the low velocity layer and unfavourable incidence angles resulting in poor focal coverage. Deeper events presented correct components solutions however, events with non-DC components proved unstable at these depths. Due to this characteristic and the non-DC nature of mine tremors, MT inversion results should be interpreted cautiously and not relied upon without supplementary information. If MT inversion is performed under complex geological conditions evenly focal coverage should be required to get the most reliable components results.

The Bogdanka mine network should not be used for routine MT inversion without supplementary information. Tests on the Bogdanka network produced accurate component solutions only for events deeper than 2 km, which are unlikely in the mining area. Additionally, the instability of solutions for non-DC events renders these results unreliable. A thick low-velocity layer contributes to unstable and nonphysical solutions. Compared to the test results from the Rudna mine, examining the influence of a detailed near-surface velocity model is essential to determine if its inclusion can enhance MT solution quality.

Since MT inversion is a common tool in seismology, the P-wave amplitude inversion method has limitations users need to consider. It restricts the use of data with a high noise-to-signal ratio and events at depths not exceeding the maximum event-station distance. For triggered seismicity, even a 20% noise level should allow for reliable MT inversion if deeper sources with predominant shearing components are observed. Mining conditions because of the shallow sources require lower noise contamination. Understanding the applied velocity models is crucial, as a high velocity gradient can lead to incorrect component determination, even if the solution appears correct.

The focal coverage is crucial for a reliable MT solution, especially in the case of mining tremors with high non-DC components. High-rate GNSS proved useful for calculating the seismic moment tensor of anthropogenic earthquakes with magnitudes under 4.0. Events similar to the analysed earthquakes could be recorded by HR-GNSS at an epicentral distance of about 7-8 km. The use of HR-GNSS can supplement the seismic network to achieve a more reliable moment tensor when seismic data is lacking or azimuthal gap cause unfavourable focal coverage.

The far-field assumption is widely used due to its simplicity, but waveform registration on short distances within local networks implies the influence of the intermediate field terms. The distance where the influence of intermediate and far-fields equalizes depends on peak duration and P-wave velocity. Amplitudes calculated with radiation pattern coefficients and seismic moment were similar to measured amplitudes. However, amplitude differences increased with the scalar seismic moment value, and outliers were more frequent at short event-station distances. Further research is necessary to examine the intermediate field's influence on more complex mechanisms and implement site effects influence on amplitudes. Considering the intermediate field's percentage contribution to the presented calculations, its influence may significantly affect seismic moment tensor solutions. The incorrect MT solutions derived for mine networks could be caused by not assuming intermediate field influence, however, for confirmation further research is required. For seismic stations closer than 10 km to the seismic event, it's worth considering intermediate field term influence. Excluding closest stations could lead to MT instability, so it is not recommended.

In summary, the findings highlight the importance of knowing the velocity model when solving MT and identifying features of the model that can cause errors, like layers boundary or low velocity layers. The proposed method of implementing additional data from HR-GNSS demonstrates its usefulness for recording tremors above M=3.5 at close distances, which improves azimuthal coverage. Research on the influence of the intermediate field underscores the significance of this issue and the necessity for further investigation. Both methods can improve MT solutions especially for shallow events observed in short distances, like in mine area monitoring.

References

Aki, K., & Richards, P. G. (2002). *Quantitative Seismology* (J. Ellis, Ed.; 2nd edition). University Science Books.

Baker, C., & Young, R. P. (1997). Evidence for extensile crack initiation in point source time-dependent moment tensor solutions. *Bulletin of the Seismological Society of America*, *87*(6), 1442–1453. https://doi.org/10.1785/BSSA0870061442

Benedetti, E., Branzanti, M., Biagi, L., Colosimo, G., Mazzoni, A., & Crespi, M. (2014). Global Navigation Satellite Systems Seismology for the 2012 Mw 6.1 Emilia Earthquake: Exploiting the VADASE Algorithm. *Seismological Research Letters*, *85*(3), 649–656. https://doi.org/10.1785/0220130094

Bock, Y., Melgar, D., & Crowell, B. W. (2011). Real-Time Strong-Motion Broadband Displacements from Collocated GPS and Accelerometers. *Bulletin of the Seismological Society of America*, *101*(6), 2904–2925. https://doi.org/10.1785/0120110007

Cesca, S., Buforn, E., & Dahm, T. (2006). Amplitude spectra moment tensor inversion of shallow earthquakes in Spain. *Geophysical Journal International*, *166*(2), 839–854. https://doi.org/10.1111/J.1365-246X.2006.03073.X/2/166-2-839-FIG012.JPEG

Cesca, S., Rohr, A., & Dahm, T. (2013). Discrimination of induced seismicity by full moment tensor inversion and decomposition. *Journal of Seismology*, *17*(1), 147–163. https://doi.org/10.1007/S10950-012-9305-8/FIGURES/8

Dahm, T., & Brandsdóttir, B. (1997). Moment tensors of microearthquakes from the Eyjafjallajökull volcano in South Iceland. *Geophysical Journal International*, *130*(1), 183–192. https://doi.org/10.1111/J.1365-246X.1997.TB00997.X

Dziewoński, A. M., Chou, T. A., & Woodhouse, J. H. (1981). Determination of earthquake source parameters from waveform data for studies of global and regional seismicity. *Journal of Geophysical Research: Solid Earth*, *86*(B4), 2825–2852. https://doi.org/10.1029/JB086IB04P02825

Ekström, G., Nettles, M., & Dziewoński, A. M. (2012). The global CMT project 2004–2010: Centroid-moment tensors for 13,017 earthquakes. *Physics of the Earth and Planetary Interiors*, *200–201*, 1–9. https://doi.org/10.1016/J.PEPI.2012.04.002

Fletcher, J. B., & McGarr, A. (2005). Moment Tensor Inversion of Ground Motion from Mining-Induced Earthquakes, Trail Mountain, Utah. *Bulletin of the Seismological Society of America*, *95*(1), 48–57. https://doi.org/10.1785/0120040047

Frohlich, C. (1995). Characteristics of well-determined non-double-couple earthquakes in the Harvard CMT catalog. *Physics of the Earth and Planetary Interiors*, *91*(4), 213–228. https://doi.org/10.1016/0031-9201(95)03031-Q

Gahalaut, K., Tuan, T. A., & Purnachandra Rao, N. (2016). Rapid and delayed earthquake triggering by the song tranh 2 reservoir, Vietnam. *Bulletin of the Seismological Society of America*, *106*(5), 2389–2394. https://doi.org/10.1785/0120160106

Gao, Z., Li, Y., Shan, X., & Zhu, C. (2021). Earthquake magnitude estimation from high-rate gnss data: A case study of the 2021 mw 7.3 maduo earthquake. *Remote Sensing*, *13*(21), 4478. https://doi.org/10.3390/RS13214478/S1

Gibowicz, S. J., & Kijko, Andrzej. (1994). *An introduction to mining seismology*. 399.

Gu, C., Marzouk, Y. M., & Nafi Toksöz, M. (2018). Waveform-based Bayesian full moment tensor inversion and uncertainty determination for the induced seismicity in an oil/gas field. *Geophysical Journal International*, *212*(3), 1963–1985. https://doi.org/10.1093/GJI/GGX517

Hardebeck, J. L., & Shearer, P. M. (2002). A New Method for Determining First-Motion Focal Mechanisms. *Bulletin of the Seismological Society of America*, *92*(6), 2264–2276.

Hasegawa, H. S., Wetmiller, R. J., & Gendzwill, D. J. (1989). Induced seismicity in mines in Canada—An overview. *Pure and Applied Geophysics*, *129*(3), 423–453. https://doi.org/10.1007/BF00874518

Hudson, J. A., Pearce, R. G., & Rogers, R. M. (1989). Source type plot for inversion of the moment tensor. *Journal of Geophysical Research: Solid Earth*, *94*(B1), 765–774. https://doi.org/10.1029/JB094IB01P00765

Ilieva, M., Rudziński, Ł., Pawłuszek-Filipiak, K., Lizurek, G., Kudłacik, I., Tondaś, D., & Olszewska, D. (2020). Combined Study of a Significant Mine Collapse Based on Seismological and Geodetic Data—29 January 2019, Rudna Mine, Poland. *Remote Sensing 2020, Vol. 12, Page 1570*, *12*(10), 1570. https://doi.org/10.3390/RS12101570

Jechumtálová, Z., & Šílený, J. (2005). Amplitude ratios for complete moment tensor retrieval. *Res. Lett*, *32*, 22303. https://doi.org/10.1029/2005GL023967

Jost, M. L., & Herrmann, R. B. (1989). A Student's Guide to and Review of Moment Tensors. *Seismological Research Letters*, *60*(2), 37–57. https://doi.org/10.1785/GSSRL.60.2.37

Kagan, Y. Y. (1991). 3-D rotation of double-couple earthquake sources. *Geophysical Journal International*, *106*(3), 709–716. https://doi.org/10.1111/J.1365-246X.1991.TB06343.X

Kokowski, J., & Rudziński, Ł. (2023). Estimation of location errors for local seismic network in an area with intense and weak seismicity. *Geophysical Journal International*, *234*. https://doi.org/10.1093/gji/ggad102

Kozłowska, M. (2013). Analysis of spatial distribution of mining tremors occurring in Rudna copper mine (Poland). *Acta Geophysica*, *61*(5), 1156–1169. https://doi.org/10.2478/S11600-013-0137-X/METRICS

Kravanja, S., Panza, G., & Šílený, J. (2002). Robust retrieval of seismic point source time function. *Geophysical Journal International*, *136*, 385–394. https://doi.org/10.1046/j.1365-246X.1999.00729.x

Kudłacik, I., Kapłon, J., Lizurek, G., Crespi, M., & Kurpiński, G. (2021). High-rate GPS positioning for tracing anthropogenic seismic activity: The 29 January 2019 mining tremor in Legnica- Głogów Copper District, Poland. *Measurement*, *168*, 108396. https://doi.org/10.1016/J.MEASUREMENT.2020.108396

Kudłacik, I., Tymińska, A., Lizurek, G., Kapłon, J., & Paziewski, J. (2023). High-rate GNSS data in seismic moment tensor inversion: application to anthropogenic earthquakes. *Geomatics, Natural Hazards and Risk*, *14*(1). https://doi.org/10.1080/19475705.2023.2232084

Kuge, K., & Lay, T. (1994). Data-dependent non-double-couple components of shallow earthquake source mechanisms: Effects of waveform inversion instability. *Geophysical Research Letters*, *21*(1), 9–12. https://doi.org/https://doi.org/10.1029/93GL03294

Kwiatek, G., Martínez-Garzón, P., & Bohnhoff, M. (2016). HybridMT: A MATLAB/Shell Environment Package for Seismic Moment Tensor Inversion and Refinement. *Seismological Research Letters*, *87*(4), 964–976. https://doi.org/10.1785/0220150251

Li, X., Zheng, K., Li, X., Liu, G., Ge, M., Wickert, J., & Schuh, H. (2019). Real-time capturing of seismic waveforms using high-rate BDS, GPS and GLONASS observations: the 2017 Mw 6.5 Jiuzhaigou earthquake in China. *GPS Solutions*, *23*(1), 1–12. https://doi.org/10.1007/S10291-018-0808-9/FIGURES/10

Lizurek, G., Leptokaropoulos, K., Wiszniowski, J., Van. Giang, N., Nowaczyńska, I., Plesiewicz, B., Van, D. Q., & Tymińska, A. (2021). Seasonal trends and relation to water level of reservoir-triggered seismicity in Song Tranh 2 reservoir, Vietnam. *Tectonophysics*, *820*, 229121. https://doi.org/10.1016/J.TECTO.2021.229121

Lizurek, G., Rudziński, Ł., & Plesiewicz, B. (2015). Mining induced seismic event on an inactive fault. *Acta Geophysica*, *63*(1), 176–200. https://doi.org/10.2478/S11600-014-0249-Y/METRICS

Lizurek, G., & Wiejacz, P. (2011). Moment Tensor Solution and Physical Parameters of Selected Recent Seismic Events at Rudna Copper Mine. *GeoPlanet: Earth and Planetary Sciences*, *3*, 11–19. https://doi.org/10.1007/978-3-642-19097-1_2/FIGURES/9

Lizurek, G., Wiszniowski, J., Giang, N. V., Van, D. Q., Dung, L. V., Tung, V. D., & Plesiewicz, B. (2019). Background seismicity and seismic monitoring in the Lai Chau reservoir area. *Journal of Seismology*, *23*(6), 1373–1390. https://doi.org/10.1007/S10950-019-09875-6/FIGURES/11

Lizurek, G., Wiszniowski, J., Van Giang, N., Plesiewicz, B., & Van, D. Q. (2017). Clustering and Stress Inversion in the Song Tranh 2 Reservoir, Vietnam. *Bulletin of the*

Seismological Society of America, *107*(6), 2636–2648. https://doi.org/10.1785/0120170042

Michel, C., Kelevitz, K., Houlié, N., Edwards, B., Psimoulis, P., Su, Z., Clinton, J., & Giardini, D. (2017). The Potential of High-Rate GPS for Strong Ground Motion Assessment. *Bulletin of the Seismological Society of America*, *107*(4), 1849–1859. https://doi.org/10.1785/0120160296

Orlecka-Sikora, B., Lasocki, S., Kocot, J., Szepieniec, T., Grasso, J. R., Garcia-Aristizabal, A., Schaming, M., Urban, P., Jones, G., Stimpson, I., Dineva, S., Sałek, P., Leptokaropoulos, K., Lizurek, G., Olszewska, D., Schmittbuhl, J., Kwiatek, G., Blanke, A., Saccarotti, G., … Fischer, T. (2020). An open data infrastructure for the study of anthropogenic hazards linked to georesource exploitation. *Scientific Data 2020 7:1*, *7*(1), 1–16. https://doi.org/10.1038/s41597-020-0429-3

Philpott, K. D. (2002). Evaluation of the Bogdanka Mine, Poland. *Polish Geological Institute Special Papers*, *7*, 199–206.

Psimoulis, P. A., Houlié, N., Habboub, M., Michel, C., & Rothacher, M. (2018). Detection of ground motions using high-rate GPS time-series. *Geophysical Journal International*, *214*(2), 1237–1251. https://doi.org/10.1093/GJI/GGY198

Pugh, D. J., White, R. S., & Christie, P. A. F. (2016). Automatic Bayesian polarity determination. *Geophysical Journal International*, *206*(1), 275–291. https://doi.org/10.1093/GJI/GGW146

Ren, Y., Vavryčuk, V., Gao, Y., Wu, S., & Gan, Y. (2022). Efficiency of Surface Monitoring Layouts for Retrieving Accurate Moment Tensors in Hydraulic Fracturing Experiments. *Pure and Applied Geophysics*, *179*(9), 3341–3356. https://doi.org/10.1007/S00024-022-03122-9/FIGURES/10

Rudzinski, Ł., Cesca, S., & Lizurek, G. (2016). Complex Rupture Process of the 19 March 2013, Rudna Mine (Poland) Induced Seismic Event and Collapse in the Light of Local and Regional Moment Tensor Inversion. *Seismological Research Letters*, *87*(2A), 274–284. https://doi.org/10.1785/0220150150

Saunders, J. K., Goldberg, D. E., Haase, J. S., Bock, Y., Offield, D. G., Melgar, D., Restrepo, J., Fleischman, R. B., Nema, A., Geng, J., Walls, C., Mann, D., & Mattioli, G. S. (2016). Seismogeodesy Using GPS and Low-Cost MEMS Accelerometers: Perspectives for Earthquake Early Warning and Rapid Response. *Bulletin of the Seismological Society of America*, *106*(6), 2469–2489. https://doi.org/10.1785/0120160062

Šílený, J. (2004). Regional moment tensor uncertainty due to mismodeling of the crust. *Tectonophysics*, *383*(3–4), 133–147. https://doi.org/10.1016/J.TECTO.2003.12.007

Šílený, J. (2009). Resolution of Non-Double-Couple Mechanisms: Simulation of Hypocenter Mislocation and Velocity Structure Mismodeling. *Bulletin of the Seismological Society of America*, *99*, 2265–2272. https://doi.org/10.1785/0120080335

Šílený, J., Campus, P., & Panza, G. F. (1996). Seismic moment tensor resolution by waveform inversion of a few local noisy records—I. Synthetic tests. *Geophysical Journal International*, *126*(3), 605–619. https://doi.org/10.1111/J.1365-246X.1996.TB04693.X

Šílený, J., & Hofstetter, A. (2002). Moment tensor of the 1999 Dead Sea calibration shot: Limitations in the isotropic source retrieval without a detailed earth model. *Tectonophysics*, *356*, 157–169. https://doi.org/10.1016/S0040-1951(02)00382-7

Šílený, J., & Vavrycuk, V. (2000). Approximate retrieval of the point source in anisotropic media: numerical modelling by indirect parametrization of the source. *Geophysical Journal International*, *143*, 700–708. https://doi.org/10.1046/j.1365-246X.2000.00256.x

Sipkin, S. A. (1982). Estimation of earthquake source parameters by the inversion of waveform data: synthetic waveforms. *Physics of the Earth and Planetary Interiors*, *30*(2–3), 242–259. https://doi.org/10.1016/0031-9201(82)90111-X

Stein, S., & Wysession, M. (2003). *An Introduction to Seismology, Earthquakes, and Earth Structure*. Blackwell Publishing.

Stierle, E., Vavryčuk, V., Šílený, J., & Bohnhoff, M. (2014). Resolution of non-double-couple components in the seismic moment tensor using regional networks—I: a synthetic case study. *Geophysical Journal International*, *196*(3), 1869–1877. https://doi.org/10.1093/gji/ggt502

Teyssoneyre, V., Feignier, B., Šílený, J., & Coutant, O. (2002). Moment Tensor Inversion of Regional Phases: Application to a Mine Collapse. *Pure and Applied Geophysics - PURE APPL GEOPHYS*, *159*, 111–130. https://doi.org/10.1007/PL00001246

Toksöz, M. N., & Kehrer, H. H. (1972). Tectonic strain release by underground nuclear explolions and its effect on seismic discrimination. *Geophysical Journal of the Royal Astronomical Society*, *31*(1–3), 141–161. https://inis.iaea.org/search/search.aspx?orig_q=RN:4065865

Vavryčuk, V. (2001). Inversion for parameters of tensile earthquakes. *Journal of Geophysical Research: Solid Earth*, *106*(B8), 16339–16355. https://doi.org/10.1029/2001JB000372

Vavryčuk, V. (2004). Inversion for anisotropy from non-double-couple components of moment tensors. *Journal of Geophysical Research: Solid Earth*, *109*(B7). https://doi.org/https://doi.org/10.1029/2003JB002926

Vavryčuk, V. (2015). Moment tensor decompositions revisited. *Journal of Seismology*, *19*(1), 231–252. https://doi.org/10.1007/S10950-014-9463-Y/FIGURES/11

Vavryčuk, V., Adamovà, P., Doubravová, J., & Jakoubková, H. (2017). Moment Tensor Inversion Based on the Principal Component Analysis of Waveforms: Method and Application to Microearthquakes in West Bohemia, Czech Republic. *Seismological Research Letters*, *88*(5), 1303–1315. https://doi.org/10.1785/0220170027

Vidale, J., Goes, S., & Richards, P. (1995). Near-field deformation seen on distant broadband seismograms. *Geophysical Research Letters - GEOPHYS RES LETT*, *22*. https://doi.org/10.1029/94GL02893

Wallace, T. C. (1985). A reexamination of the moment tensor solutions of the 1980 Mammoth Lakes Earthquakes. *Journal of Geophysical Research*, *90*(B13), 11171. https://www.academia.edu/50403088/A_reexamination_of_the_moment_tensor_solutions_of_the_1980_Mammoth_Lakes_Earthquakes

Wei, G., Chen, K., Zou, R., Song, J., & Li, Y. (2022). On the Potential of Rapid Moment Magnitude Estimation for Strong Earthquakes in Sichuan–Yunnan Region, China, Using Real-Time CMONOC GNSS Observations. *Seismological Research Letters*, *93*(5), 2659–2669. https://doi.org/10.1785/0220210210

Wiszniowski, J., Van Giang, N., Plesiewicz, B., Lizurek, G., Van, D. Q., Khoi, L. Q., & Lasocki, S. (2015). Preliminary results of anthropogenic seismicity monitoring in the region of song tranh 2 reservoir, central Vietnam. *Acta Geophysica*, *63*(3), 843–862. https://doi.org/10.1515/ACGEO-2015-0021/METRICS

List of figures

Figure 1 Source-type diamond plot with mechanisms with DC component decreasing by 10%. The Violet dot is a pure shearing mechanism, when red one is for a pure tensile crack with no DC component. 9
Figure 2 Seismic wave path description with the definitions of incidence and takeoff angles......13
Figure 3 The moment tensor ISO, CLVD and DC components participation in full solution depending on the tensile angle. 13
Figure 4 Source time function for Haskell fault model. 16
Figure 5 Maps for mine areas with seismicity a) Bogdanka mine, b) LGCD area. 19
Figure 6 Velocity models for Bogdanka and Rudna mine......... **Błąd! Nie zdefiniowano zakładki.**
Figure 7 Maps of seismicity for artificial reservoir areas a) Lai Chau, b) Song Tranh......**Błąd! Nie zdefiniowano zakładki.**
Figure 8 Velocity models for Song Tranh 2 and Lai Chau areas. 21
Figure 9 Jackknife single station rejection tests for all networks. Red lines in full solution for LGCD network show the nodal planes of solutions with excluded TRBC station. 23
Figure 10 Focal coverage of the MT solution in depth for different networks. 24
Figure 11 Rotation angle between full and deviatoric solution for a) Song Tranh, b) Lai Chau, c) LGCD, d) Bogdanka mine. 25
Figure 12 Synthetic tests diamond plots for LGCD, the normal fault for four noise levels and six depths. 27
Figure 13 Synthetic tests diamond plot for LGCD, reverse fault. 28
Figure 14 Synthetic tests diamond plots for Bogdanka, the normal fault for four noise levels and six depths. 30
Figure 15 Synthetic tests diamond plots for Bogdanka, reverse fault for four noise levels and six depths. 31
Figure 16 Synthetic tests diamond plots for Song Tranh, normal fault for four noise levels and eight depths. 33
Figure 17 Synthetic tests diamond plots for Song Tranh, reverse fault for four noise levels and eight depths. 34
Figure 18 Synthetic tests diamond plots for Lai Chau, normal fault for four noise levels and eight depths. 36
Figure 19 Synthetic tests diamond plots for Lai Chau, reverse fault for four noise levels and eight depths. 37
Figure 20 Full moment tensor solutions for 2019 and 2020 events a) pure SM solution and all GNSS applied data solution for 2019, b) SM solution and solution with additional GNSS station for 2020 event, c)solutions for different configurations of applied GNSS data in 20219 event, d)source-type plots for different solutions for 2019 and 2020 events. 39
Figure 21 Detailed MT solutions for the 2019 event with different sets of seismic and HR-GNSS data. 41
Figure 22 Detailed MT solutions for the 2020 event with two different sets of seismic and HR-GNSS data. 42

Figure 23 Maximum synthetic P-wave amplitude for different depths and magnitudes in the range 2.5 to 4.5 presented for three velocity models: real velocity model, isotropic, and gradient.........43
Figure 24 Far and intermediate fields influence depending on the source-station distance with radiation pattern coefficient equal 1 for far-field and 4 for intermediate field. Plots for a) LGCD, b) Song Tranh. 45
Figure 25 Amplitudes calculated based on far and intermediate field assumptions for four selected events from the LGCD area. 46
Figure 26 Amplitudes calculated based on far and intermediate field assumptions for four selected events from the Song Tranh area. 47
Figure 27 Histograms of the intermediate field amplitude part in total amplitude for two cases. .47
Figure 28 The LGCD calculated and measured amplitude differences compared with depth, moment magnitude and event-station distances. 48
Figure 29 The Song Tranh calculated and measured amplitude differences compared with depth, moment magnitude and event-station distances. 49